SUPRAMOLECULAR SELF-ASSEMBLY OF GOLD RECTANGLES

WOO MING SHUE, MICHELLE
(B.Sc. (Hons.), NUS)

A THESIS SUBMITTED

FOR THE DEGREE OF MASTER OF SCIENCE

DEPARTMENT OF CHEMISTRY

NATIONAL UNIVERSITY OF SINGAPORE

2009

ACKNOWLEDGEMENTS

I would like to express my deepest gratitude to my supervisor A/P Yip Hon Kay, John and co-supervisor A/P Loh Kian Ping for their guidance and helpful advice throughout the course of this project.

I would like to thank Prof. Koh Lip Lin and Ms. Tan Geok Kheng for solving the crystal structures. I also thank the staffs in the NMR, Elemental Analysis and Mass Spectrometry Laboratories.

I would like to thank Ms. Wang Yuanyuan for her help and assistance in this project especially in the mounting of crystals for X-ray crystallographic analyses.

I would like to thank Mr. Zhong Yulin for his guidance in the XPS experiments.

I would also like to thank my friends in my research group, Mr. Hu Jian, Mr. Soh Wei Kian, and Mr. Nguyen Minh Hai for their help in one way or another.

Special thanks go out to Ms. Ng Zhaoyue and my other friends in Laboratory under LT 23 for the happiness they have brought to me.

I am also grateful to NUSNNI and ONDL for lending their facilities.

I am thankful to my parents, sister and friends who have given me their support.

Last but not least, I would like to thank The National University of Singapore for the research scholarship.

TABLE OF CONTENTS

Chapter 1. Introduction

Chapter 2. Self Assembly of Gold Rectangles

Chapter 3. Surface Techniques and Characterization

SUMMARY

Self-assembly of supramolecular complexes has been an on going research area in our laboratory. We have synthesized several complexes with interesting spectroscopy properties and potential applications in chemical sensing. To further our research in this area, we have designed and synthesized new supramolecular complexes.

Another important and fundamental process in surpramolecular chemistry is self-organization. A self-organized molecular layer could provide promising materials for the construction of nanodevices that cannot be prepared by conventional microfabrication. As such, we begin to explore the ordered deposition of self-assembled species on surfaces.

The self-assembly of supramolecular complexes particularly Au^I metallacycles have been reviewed in Chapter 1.

In this work, two new Au^I molecular rectangles have been synthesized. The syntheses and characterizations are being described in Chapter 2. The molecular rectangles possess large cavities. The first molecular rectangle, $[Au_4(\mu\text{-PAnP})_2(\mu\text{-DPE})_2](OTf)_4$, has a cavity of 8.10 x 19.09 Å. The second molecular rectangle, $[Au_4(\mu\text{-PAnP})_2(\mu\text{-BPE})_2](OTf)_4$, has a cavity of 9.20 x 18.66 Å. The electronic absorption and emission spectroscopy of both rectangles have also been studied. Both molecular rectangles are capable of host-guest interactions with aromatic guests such as 9-bromoanthrancene, naphthalene, phenanthrene and pyrene. The emissions of the Au^I rectangles were quenched upon guest binding. The binding constants with such guests were reported.

Another Au^I molecular rectangle, $[Au_4(\mu\text{-PAnP})_2(\mu\text{-bipy})_2](OTf)_4$, which was previously synthesized by our laboratory was used to form a self-organized monolayer on several

different substrates. The molecular layer was characterized by several surface techniques such as X-ray photoelectron spectroscopy, ellipsometry, surface fluorescence and scanning tunneling microscopy. The results were presented in Chapter 3.

ABBREVIATIONS

An	anthracene
A.U.	arbituary units
BDD	boron doped diamond
bipy	4,4’-bipyridyl
BPE	1,2-bis(4-pyridyl)ethane
Br-An	9-bromoanthrancene
DPE	1,2-di(4-pyridyl)ethylene
ESI-MS	electrospray ionization mass spectroscopy
HOPG	highly oriented pyrolytic graphite
Nap	naphthalene
NMR	nuclear magnetic resonance
OTf	trifluoromethanesulfonate
PAnP	9,10-bis(diphenylphosphino)anthracene
Phen	phenanthrene
Py	pyrene
STM	scanning tunneling microscopy
u-NCD	undoped nanocrystalline diamond
XPS	x-ray photoelectron spectroscopy

LIST OF TABLES

LIST OF FIGURES

CHAPTER 1

INTRODUCTION

1.1 Supramolecular complexes

The self-assembly of discrete supramolecular complexes, incorporating building blocks with potentially useful properties, has received considerable attention in recent years. Lehn has described supramolecular chemistry as an information science in which molecular subunits that contain the necessary information self-assemble into large specific structures.[1] Complementary and explicit interaction of individual components with the appropriate symmetry and geometry generated the product assembly.

Recently, there is a growing interest in the inorganic counterparts of cyclophane, often known as metallacyclophanes or metallacycles. This class of compounds is commonly synthesized by the coordination directed self-assembly of transition metal and multitopic ligands.[2-4] This synthetic methodology has been proved to be very versatile and comprehensive as based on it a myriad of molecular triangles,[5-13] squares,[12, 14, 15] rectangles,[16, 17] pentagons,[18] hexagons,[19, 20] marcocycles,[21, 22] polyhedrons and cages[23-26] have been created.

Many metallacycles are composed of late transition metals, especially Pd^{II}, Pt^{II}, Ag^{I} and Au^{I}. One of the advantages of late transition metal ions is that the complexes of these metal ions usually have low coordination number and the numbers of possible coordination geometry of the complexes are limited. For example, Pd^{II} and Pt^{II} are known to form square planar four coordinate complexes, whereas Ag^{I} and Au^{I} prefer two-linear coordination.[14, 27]

1.1.1 Au (I) Metallacycles

The preference for Au^I complexes to adopt a two coordinate linear geometry makes it an ideal metal for the formation of large macrocycles. The versatility of Au^I in forming metallacycles will be illustrated with several selected examples.

It is known that ring-like structures can be constructed from a combination of Au^I centers and bidentate ligands such as diphosphines. Eight- to ten-membered dinuclear Au^I complexes with bidentate phosphines, thiols, ylides or dialkyldithiopcarbamates, and fourteen membered rings with dithiol and diphosphine ligands have been reported.[28, 29] Such compounds not only have interesting structural features but also exhibit rich photochemical properties.

An example is a simple Au^I loop, $[Au(dpdo)]ClO_4$ which was constructed from an exotic diphosphine dpdo (1,8-bis(diphenylphosphino)-3,6-dioxaoctane).[30] The folding of the long backbone of the diphosphine allowed the ligand to coordinate to the metal ions in a trans-fashion. The combination of the ligand and Au^I led to the formation of a 11-membered ring. This Au^I complex itself is non-emissive but displays strong photoluminescence upon the addition of nucleophiles.

Another interesting example of Au^I metallacycle is a binuclear Au^I complex $[Au_2(dpy)_3]^{2+}$ done by Shieh *et al* as shown in Figure 1.1 (dpy = 2,6-bis(diphenylphosphino)pyridine).[31] This complex has a cavity which was formed by bridging two Au^I ions with three dpy ligands. The intramolecular Au-Au separation is 4.866(2)Å and the complex displays emission bands centered at 415 and 520 nm at room temperature.

Figure 1.1 ORTEP of binuclear Au^I complex $[Au_2(dpy)_3]^{2+}$ (Copyright permission granted by RSC)

Recently, our laboratory has reported a luminescent gold rectangle, $[Au_4(\mu\text{-PAnP})_2(\mu\text{-bipy})_2](OTf)_4$ (PAnP = 9,10-bis-(diphenylphosphineo)anthracene, bipy = 4,4'-bipyridine). This molecular rectangle has a large cavity and is capable of host-guest interactions.[32]

Au^I metallacycles have presented many interesting photochemistry and promising applications such as in the area of host-guest chemistry.

1.1.2 Host-Guest Interactions

Supramolecular assemblies have been used as sensors,[33, 34] catalysts,[35, 36] and host-guest materials.[37-39] A major facet of host-guest chemistry is to understand molecular recognition, a multitude of processes and interactions that lies at the heart of many biological phenomena.[40] Traditionally, the field has been dominated by organic molecules and the host-guest chemistry of receptors such as crown ether,[41] cryptand[42] and cyclophanes[43] have been extensively studied.

Maverick first demonstrated that self-assembled metallacycles have the ability of acting as receptors for organic molecules in 1984.[44] He reported the study of the binding of 1,4-diazabictclo[2,2,2]octane to a cofacial dicopper(II) macrocycle. Fujita *et al* showed that the self-assembled molecular square $[M_4(en)_4(\mu\text{-bipy})_4](NO_3)_8$ (M = Pd^{II}, Pt^{II}, en = 1,2-diaminoethane, bipy = 4,4'-bipyridine) binds to neutral and anionic aromatic molecules.[14, 45] Later studies showed that binuclear Pd^{II} macrocycles which contain flexible and electron-deficient linkers could exhibit shape selectivity and higher affinity for electron-rich aromatics.[46] The guest binding properties of metallacycles of Zn^{II},[47] Ru^{II},[48] Pd^{II},[49] Pt^{II},[15, 49] Rh^{I},[50] Re^{I},[12, 51] and Os^{VI}[52-54] have been extensively studied. The metallacycles form inclusion complexes with guest such as substituted benzene[46-48] and anthracenes. The binding invokes π-π interactions between the aromatic rings of the host and guests.[47] However, in some cases, other interactions such as hydrogen bonding,[17, 52-54] metal-ligand coordination,[55] metal-metal bonding[56] are also involved in the stabilization of the host-guest complexes. Aromatic guests are usually incarcerated in the cavity of the metallacycles.[47, 56]

The principle of stereoelectronic complementarity states that for a receptor to display guest selectivity, its geometry and the electronic properties have to be complementary to those of the designated guest. In addition, preorganization of the binding site also favors the complexation by minimizing the free energy required for conformation changes.[57] Based on these principles, molecular rectangles which contain extended π-surface aromatic ligands could be selective receptors for planar polyaromatic molecules.

Reported syntheses of molecular squares are more common than molecular rectangles.[16, 17, 51] One of the reported molecular square is shown in Figure 1.2. Some reported examples of molecular rectangles are binuclear Pd^{II} complexes which can be assembled into [2]catenanes.[16] Other examples include $[M_4(CO)_{12}(\mu\text{-bipy})(bipm)_2]$ (M = Mn^{I} and Re^{I})[51, 58] and $[Pt_4(PEt_3)_8(\mu\text{-anth}^{2-})_2(\mu\text{-L})]^{4+}$ (anth = anthracene-1,8-diyl, L = bipy, 1,4-bis(4-ethynlpyridyl)benzene, 2,5-bis(4-ethynylpyridyl)furan or BPE). [59, 60]

Figure 1.2 Osmium (VI)-bridged molecular square with guest *N,N,N'N'*-tetramethylterephthalamide. (Copyright permission granted by ACS)

1.2 Self-Organized Monolayer

Self-organization[61] and self-assembly[62] are natural phenomenon, which can be observed in many biological, chemical, and physical processes and has recently been widely used as an efficient and versatile tool for creating nanostructures at surfaces. These processes play an important role in the so-call "bottom-up" strategy of nanofabrication. Therefore, understanding how molecules are organized on solid surfaces is important, both from a fundamental and applied perspective, for the construction of surface molecular nanostructures and nanodevices.[63-66]

Considerable effort has been made to distribute and/or arrange molecules into thin films or on surface, with the expectation that the new fabricated film or surface will posses beneficial properties.[64-69] When molecules spontaneously adsorb in a monomolecular layer on surfaces, they are known as “self-assembled monolayers” (SAMs).[61] The assembly process is being dictated by well-defined intermolecular interactions and interactions between adsorbate and substrate.[70] Self-assembly on surfaces has tended to involve the adsorption of alkylthiols on Au surfaces, a phenomenon first discovered in 1983 by Nuzzo and Allara.[71]

As with a self-assembled monolayer, a self-organized monolayer achieves a local decrease in entropy through a higher degree of order as a result of lowering the energy by optimizing weak intermolecular or molecule-substrate interactions. As it relies on only weak interactions, rather than covalent bonds, a self-organized monolayer is less likely to be in a global energy minimum. In the series of surface ordering processes such as self-assembly, self-organization, self-construction, or self-repair, self-organization comes closest to the “reaction” conditions recognized in supramolecular synthesis. It is, so to speak, a supramolecular, two dimensional (2D) assembly supported by a surface.[70]

For the last two decades, supramolecular chemistry has used the advantages of self-assembly to control the synthesis of non-covalent structures in solution.[72, 73] However, there is still limited knowledge about how to transfer the principles that govern the solution synthesis directly to the construction of well-defined supramolecular structures on surfaces.[63, 74, 75]

Some examples of self-organized monolayer are done by Hipps et al, who prepared a self-organized 2D bifunctional structure on a Au (111) with NiTPP [nickel

(II)tetraphenyl-21H,23H-porphine] and F16CoPc [cobalt(II) hexadecafluoro-29H,31H-phthalocyanine].[64, 65]

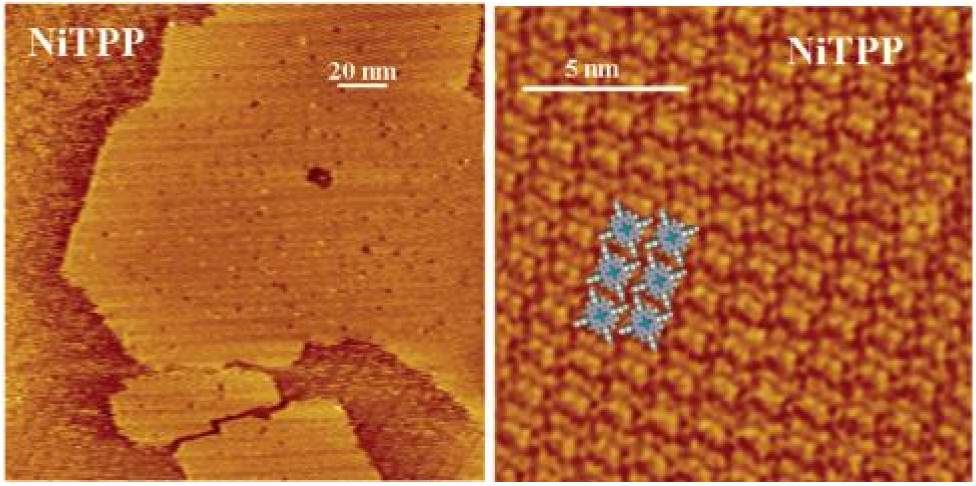

Figure 1.3 Constant current STM images of NiTPP adsorbed on Au(111) imaged under UHV conditions. (Copyright permission granted by ACS)

1.2.1 Preparation of Self-Organized Monolayer

Various methods have been used to prepare monolayer, depending on the properties of the compound and the substrate used. A common way is to immerse the substrate into a solution containing the molecules. This method is most commonly used to prepare alkylthiols on Au (111) substrate. However, in formation of alkylthiols SAM, chemisorption is a critical step. Other systems which utilize weak interactions rely on physisorption and have also been prepared by the same procedures.[76, 77]

Solution-casting or drop-casting is a simple method of preparing self-organized monolayer. It is usually done on highly oriented pyrolytic graphite. However, the formation of monolayer depends on the concentration of the solution used. It is critical to know the optimum concentration needed to form a monolayer on the substrate.[76]

Vapor deposition or evaporation of molecules onto the substrate is another technique used to form monolayer. It has to be performed under ultrahigh vacuum conditions. This technique has a constraint in that the molecules are limited to those which can be vaporized.[78]

1.2.2 Intermolecular and Molecule-Substrate Interactions

In supramolecular chemistry, non-covalent interactions play a predominant role. These interactions can be utilized in the self-organization of molecular compounds on various surfaces.

The precise structure of the long range ordering of those adsorbed molecular layers depends in the delicate balance between molecule-molecule and molecule-substrate interactions. On a graphite surface in a dry environment, the molecule-molecule interactions dominate over the molecule-substrate interactions. The supramolecular compounds are prevented from lying flat on the surface and instead the molecules form a lamellar, stacked structure that can be imaged with scanning tunneling microscope (STM) at a high lateral resolution.[79]

Later work by Stang et al looked at self-assembled supramolecular metallocyclic rectangle, cyclobis[(1,8-bis(transPt(PEt_3)$_2$)anthracene)(1,4'-bis(4-ethynylpyridyl) benzene](PF_6)$_4$ being adsorbed on graphite and Au (111) surface. Using the STM, it was observed that the rectangles stand vertically with their long edge on the underlying HOPG surface, while on a Au (111) surface, the macrocycles lies flat.[76]

1.2.3 Characterization

Sophisticated surface analytical and structural techniques have led to a detailed understanding of molecular packing in SAMs particularly in films composed of alkylthiols adsorbed on the Au (111) surface.[80] SAMs have been thoroughly characterized using a large number of surface analytical tools. Among the most frequently used techniques are infrared spectroscopy,[81] ellipsometry, x-ray photoelectron spectroscopy (XPS),[82] electrochemistry, and scanning probe measurements.[83]

In contrast, surface characterizations of self-organized monolayer of supramolecular assemblies have not been well studied and are mainly confined to scanning probe measurements such as atomic force microscopy (AFM)[84-86] and scanning tunneling microscopy (STM).[76, 77]

1.3 Objectives

As mentioned above, Au^I metallacycles presents many interesting properties and potential applications. However, Au^I molecular rectangles remain uncommon. Our group has synthesized an anthracene-based bidentate ligand: 9,10-bis(diphenylphosphone)anthracene (PAnP) which can impart luminescence to its metal complexes.[22] It also has flexible anthracenyl backbone which enables its metal analogue $[Au_2(\mu\text{-PAnP})]^{2+}$ to act as a molecular "clip" in assembling molecular rectangles. One such rectangle has been synthesized by assembling two molecular "clip" with two bipy ligands.[32]

In this thesis, one of the objectives is to synthesis two new Au^I molecular rectangles with larger cavity. Their spectroscopy and host-guest chemistry will also be explored.

Unlike many examples of self-organization of organic molecules,[87, 88] self-organization of supramolecular assemblies on surfaces is an area which remains relatively untouched. Supramolecular assemblies possess magnetic, photophysical, electronic, and/or redox properties that may not be accessible from purely organic systems.[89-92] Hence, there lies the challenge to assemble and characterize these monolayers.

As an ongoing effort to understand self-organized monolayer of supramolecular assemblies, a Au^{I} molecular rectangle will be assembled on several substrates and these monolayers will be characterized by XPS, ellipsometry, surface fluorescence and STM. In the next chapter, we will start with synthesis of the two new Au^{I} molecular rectangles and their properties, followed by the preparation and characterization of self-organized monolayer of the Au^{I} molecular rectangle.

CHAPTER 2

SELF-ASSEMBLY OF GOLD RECTANGLES

2.1 Introduction

Over the past two decades, metal-ligand coordination has been used to create discrete supramolecular assemblies.[93] This methodology is very established and many supramolecular assemblies can be synthesized in one-pot reactions and in high yields. They display physical properties that are generally inaccessible with their organic counterparts. Moreover, the reversible, metal-ligand bond formation facilitates error checking and self-correction.[94] The design and construction of new supramolecular entities refine our understanding of the fundamental principles of molecular self-assembly.

The interests in weak, noncovalent interactions extend to supramolecular host-guest complex. A few studies have shown that molecular squares are capable of acting as hosts for small aromatic molecules.[14, 45] These studies in basic host-guest chemistry have broad implications for technologies such as molecular sensing, separations and catalysis. In contrast, there are few examples of such studies done with molecular rectangles.

Hence, with the successful synthesis of the PAnP ligand and the molecular clip $[Au_2(\mu\text{-}PAnP)]^{2+}$, we devise to synthesis Au^I molecular rectangles with large cavity for host-guest interaction.

2.2 Experimental Section

2.2.1 Materials

$KAuCl_4$ was purchased from Oxkem and used as received. 9, 10-dibromoanthracene, butyl lithium (1.6 M solution in hexanes), chlorodiphenyl phosphine, silver triflate (AgOTf), dimethyl sulfide, 1,2-di(4-pyridyl)ethylene (DPE) and 1,2-bis(4-pyridyl)ethane

(BPE) were obtained from Aldrich and used without further purification. All of the aromatic guests were obtained from Aldrich and were purified by recrystallization from hot ethanol. All solvents used in synthesis were purified according to literature methods.[95]

2.2.2 Physical Methods

^{1}H NMR and ^{31}P NMR spectra were recorded on a Bruker ACF300 (300 MHz) spectrometer or Bruker AMX500 (500 MHz) spectrometer, with ^{1}H chemical shifts (δ) given in ppm relative to residual nondeuterated CDCl3 (δ 7.26). ^{31}P chemical shifts were reported relative to external 85% aqueous H_3PO_4 (δ 0.0). Electrospray ionization mass spectra (ESI-MS) were measured on a Finnigan MAT 731 LCQ spectrometer. UV-vis spectra were recorded on a Hewlett-Packard 8452A diode array spectrometer and fluorescence spectra were recorded on a Perkin-Elmer LS55B spectrofluorophotometer. The averaged optical path length for the emitting light is 1 cm. Luminescene quantum yield was referenced to anthracene in chloroform ($\Phi_{\mathrm{std}} = 0.27$) and calculated according to the following equation:

$$\Phi_{em} = \Phi_{std}\left(\frac{I}{A}\right)\left(\frac{A_{std}}{I_{std}}\right)\left(\frac{n}{n_{std}}\right)$$

where Φ_{em} is the radiative quantum yield of the sample, Φ_{std} is the radiative quantum yield of the standard, I and I_{std} are the integrated emission intensities of the sample and standard, A and A_{std} are the absorbances of the samples and standard at the excitiation wavelength, and n and n_{std} are the refractive indexes of the sample and standard solutions (pure solvents were assumed). Elemental analyses were carried out by elemental analysis laboratory in National University of Singapore.

2.2.3 X-ray Crystallography

The diffraction experiments were carried out on a Bruker AXS SMART CCD three-circle diffractometer with a sealed tube at 20ºC using graphite-monochromated Mo Kα radiation (λ = 0.71073 Å). The software used were SMART[96] for collecting frames of data, indexing reflection and determination of lattice parameters, SAINT[96] for integration of intensity of reflections and scaling, SADABS[97] for empirical absorption correction, and SHELXTL[98] for space group determination, structure solution and least-squares refinements on $|F|^2$. The crystals were mounted in capillaries for the diffraction experiments. Anisotropic thermal parameters were refined for rest of the non-hydrogen atoms. The hydrogen atoms wre placed in their ideal positions.

2.2.4 Fluorescence Quenching Studies

The emission spectra of CH_3CN solutions containing the same concentration of **1** or **2** $[H]_t$ but different concentrations of the aromatic guests were recorded. The excitation wavelength was chosen to be 420 nm so as to minimize the interference due to the emission of the guests and to optimize signals. The intensity I_H was plotted against the concentration of the guest $[G]_t$ and the binding constants K_Q were fitted by nonlinear least-squares regression with equation 1.

$$I_H = I_H^{\circ} - [\frac{\Delta I_H}{2[H]_t}(B - \sqrt{B^2 - 4[H]_t[G]_t})] \qquad \text{eq.1}$$

$$B = [H]_t + [G]_t + \frac{1}{K_Q} \qquad \text{eq 1.1}$$

2.3 Synthesis

All reactions were carried out in an atmosphere of nitrogen using standard Schlenk techniques. 9,10-bis(diphenylphosphino)anthracene (PAnP)[22] and $Au_2(\mu\text{-PAnP})Cl_2$[100] were synthesized according to reported methods.

2.3.1 Synthesis of $[Au_4(\mu\text{-PAnP})_2(\mu\text{-DPE})_2](OTf)_4$ (1)

To 35 mL of degassed dichloromethane in a 150 mL Schlenk flask, $Au_2(\mu\text{-PAnP})Cl_2$ (0.0791 g, 0.0782 mmol) was added with three mol. equiv of $AgCF_3SO_3$ (0.0603 g, 0.234 mmol) and the solution was stirred in darkness for 1h. The solution was filtered to remove AgCl and the filtrate was transferred to 35 mL of degassed dichloromethane/methanol (8:2, v/v) solution of 1,2-di(4-pyridyl)ethylene (0.0142 g, 0.0782 mmol). The solution was stirred for another 3h. The resulting reaction mixture was filtered and the volume of the filtrate was reduced to 5 mL and excess diethylether was added to precipitate the yellow product. Diffraction quality crystals were obtained from layering of hexane into a CH_2Cl_2/MeOH (8:2, v/v) solution of the product in an NMR tube. Yield 0.09g (84.9%). The ^1H and $^{31}P\{^1H\}$ NMR spectra and the ESI-MS spectra will be discussed later. Anal Calcd for $C_{104}H_{76}Au_4P_4N_4S_4O_{12}F_{12}$: C, 43.96; H, 2.70; N, 1.97; Found: C, 44.21; H, 3.13; N, 1.85.

2.3.2 Synthesis of $[Au_4(\mu\text{-PAnP})_2(\mu\text{-BPE})_2](OTf)_4$ (2)

To 35 mL of degassed dichloromethane in a 150 mL Schlenk flask, $Au_2(\mu\text{-PAnP})Cl_2$ (0.0761 g, 0.0752 mmol) was added with three mol. equiv of $AgCF_3SO_3$ (0.0580 g, 0.225 mmol) and the solution was stirred in darkness for 1h. The solution was filtered to remove AgCl and the filtrate was transferred to 30 mL of degassed dichloromethane solution of 1,2-bis(4-pyridyl)ethane (0.0138 g, 0.0752 mmol). The solution was stirred for another 6h. The resulting reaction mixture was filtered and the volume of the filtrate was reduced to 5 mL and excess diethylether was added to precipitate the yellow product. The compound was purified by recrystallization from layering of diethylether into a CH_2Cl_2 solution of the product in an NMR tube. Yield 0.09g (85.4%). The ^1H and $^{31}P\{^1H\}$ NMR spectra and the ESI-MS spectra will be discussed later. Anal Calcd for $C_{104}H_{80}Au_4P_4N_4S_4O_{12}F_{12}$: C, 43.89; H, 2.84; N, 1.97; Found: C, 44.07; H, 3.34; N, 1.84.

Scheme 2.1 Synthesis of of $[Au_4(\mu\text{-PAnP})_2(\mu\text{-DPE})_2](OTf)_4$ **1**

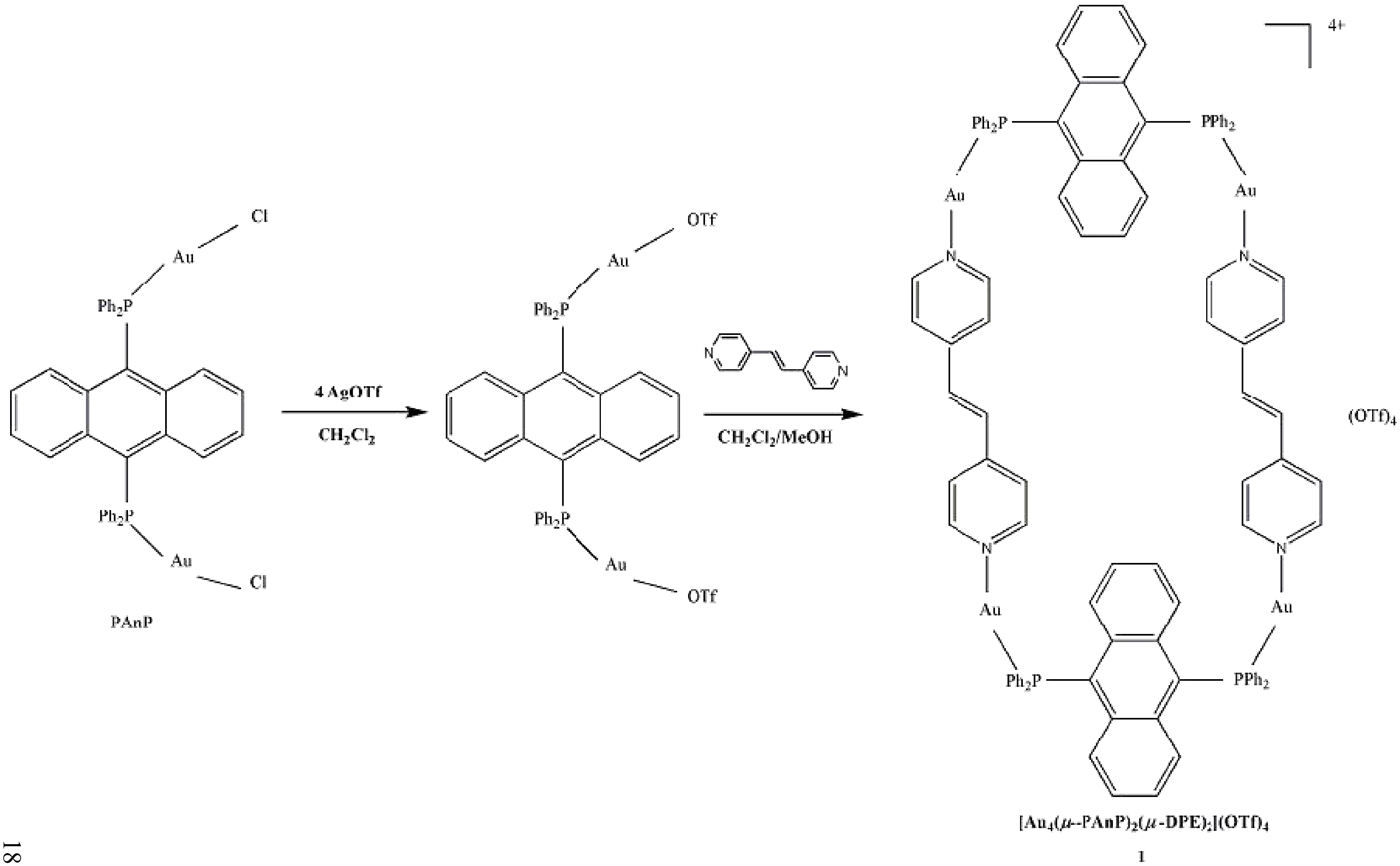

Scheme 2.2 Synthesis of $Au_4(\mu\text{-PAnP})_2(\mu\text{-BPE})_2](OTf)_4$ **2**

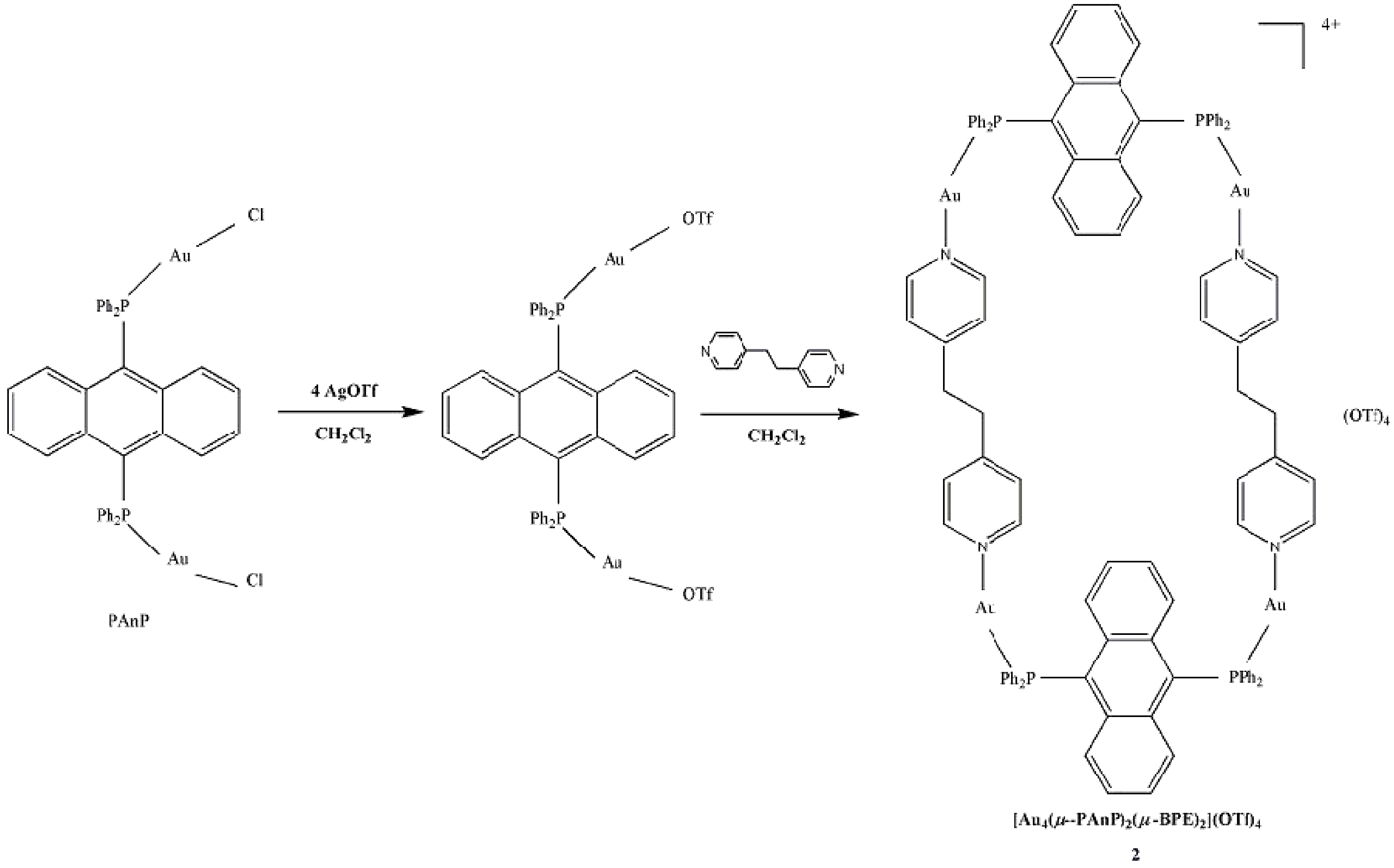

2.4 Results and Discussion

The idea of using molecular "clip" in assembling metallcycles was illustrated by the work of Stang in which an organoplatinum clip [$Pt_2(\mu\text{-anth}^{2-})(OTf)_2$] was used in the self-assembly of molecular rectangles, cages and trigonal prisms.[59, 60, 101] We have demostrated the synthesis of a gold rectangle by combining a digold "clip" $Au_2(\mu\text{-PAnP})Cl_2$ with 4,4'-bipyridine.[32] To create larger rectangles, the molecular "clip" is reacted with 1,2-di(4-pyridyl)ethylene and 1,2-bis(4-pyridyl)ethane **(Scheme 2.1 and 2.2)**. Both rectangles have been characterized by ^1H and ^{31}P NMR, ESI mass spectrometry and elemental analysis. Their structures were determined by X-ray crystallography.

2.4.1 Structure of $[Au_4(\mu\text{-PAnP})_2(\mu\text{-DPE})_2](OTf)_4$ 1

The molecular rectangle was synthesized, in high yield from a reaction between $Au_2(\mu\text{-PAnP})(OTf)_2$ and 1 mol equiv. of 1,2-di(4-pyridyl)ethylene in CH_2Cl_2/MeOH (8:2, v/v) mixture. The compound is soluble in CH_3CN, CH_2Cl_2/MeOH (8:2, v/v) mixture but sparingly soluble in CH_2Cl_2. The gold rectangle is light sensitive in solution.

The structure of the gold rectangle is characterized by the $^{31}P\{^1H\}$ and ^1H NMR. The $^{31}P\{^1H\}$ spectrum of **1** ($CDCl_3/CD_3OD$) showed a sharp singlet at 21.89 ppm (Figure 2.1) indicating that all phosphorous atoms are equivalent. The signal is shifted upfield from $Au_2(\mu\text{-PAnP})Cl_2$ by ~5.0 ppm,

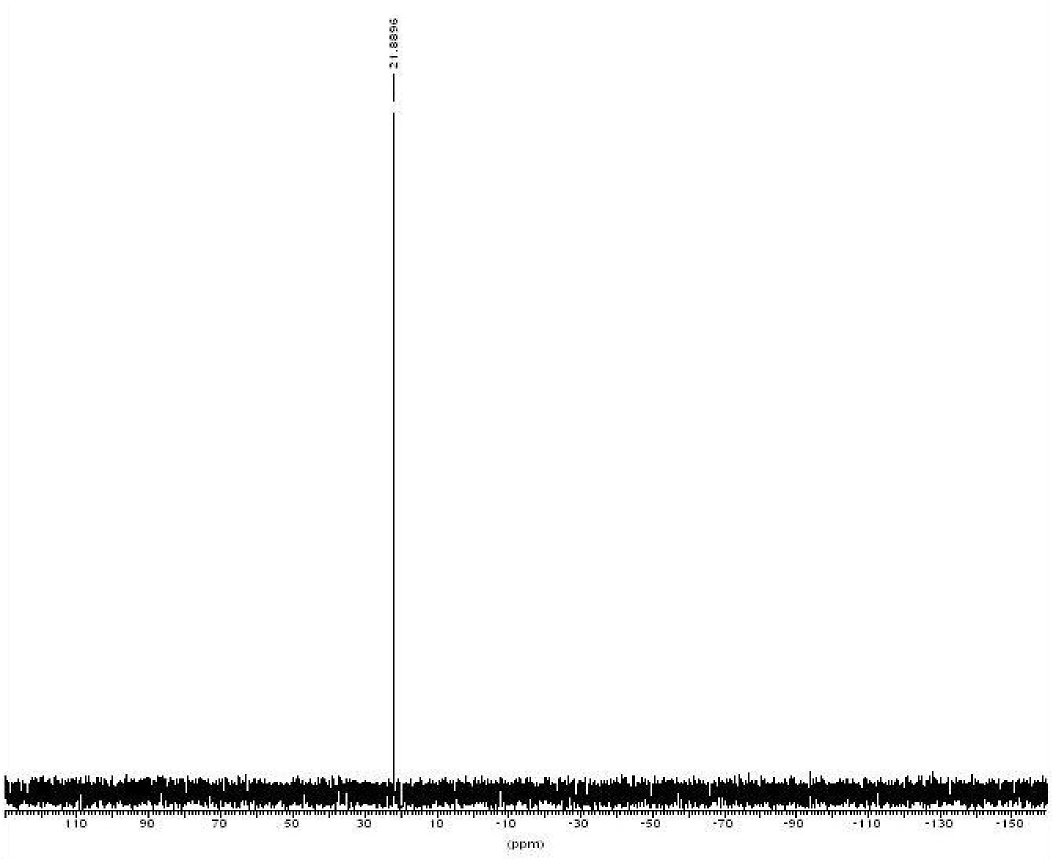

Figure 2.1 $^{31}P\{^{1}H\}$ NMR spectrum of **1** (500 MHz, $CDCl_3/CD_3OD$)

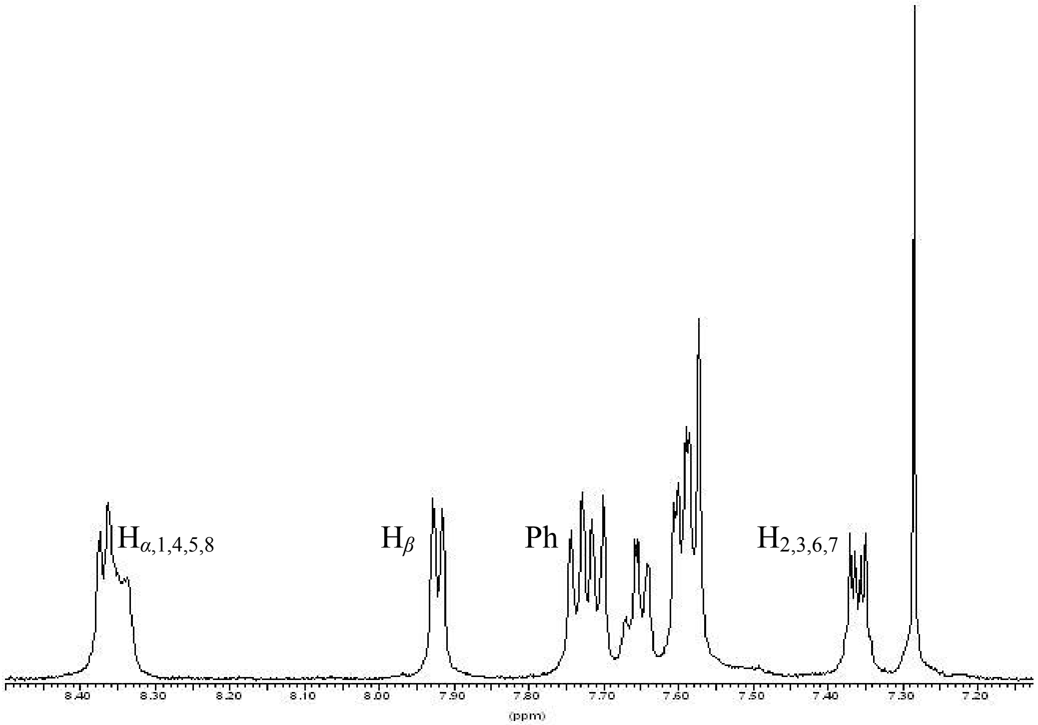

Figure 2.2 ^{1}H NMR spectrum of **1** (500 MHz, $CDCl_3/CD_3OD$)

The result suggests the formation of a discrete and highly symmetric complex.

The ^{1}H NMR spectrum shows a doublet at δ 7.92, which is due to the β-protons of the pyridyl rings (Figure 2.2). The signals for the α-protons overlap with the multiplets arising from the protons in the anthracenyl in δ 8.30 - 8.40. The multiplets in δ 7.55 - 7.80 are attributed to the phenyl rings protons. Finally, the peak at δ 7.36 is due to the protons attached to the anthracenyl ring at positions 2, 3, 6 and 7.

The ESI-MS spectrum of **1** measured in CH_2Cl_2/MeOH (8:2, v/v) showed three cluster peaks at *m/z* = 1271.06, 797.81 and 561.43 (Figure 2.3). The peak at *m/z* 797.81 is attributed to the triply charged species $[\mathbf{1} - 3\mathrm{OTf}]^{3+}$ (calcd. *m/z* 798.18). The most intense peak of the spectrum at *m/z* 1271.06 is assigned to the "half-rectangle" $[\mathrm{Au_2}(\mu\text{-PAnP})(\mathrm{DPE})\mathrm{OTf}]^{+}$ (calcd *m/z* 1271.79). The peak at *m/z* 561.43 is attributed to the ion $[\mathrm{Au_2}(\mu\text{-PAnP})(\mathrm{DPE})]^{2+}$ (calcd *m/z* 561.36). The assignments are further supported by simulated isotopic distributions (Figures 2.4 - 2.6). These results lend support to the rectangular structure of **1**. Elemental analysis of the compound also agrees well with the proposed molecular formula.

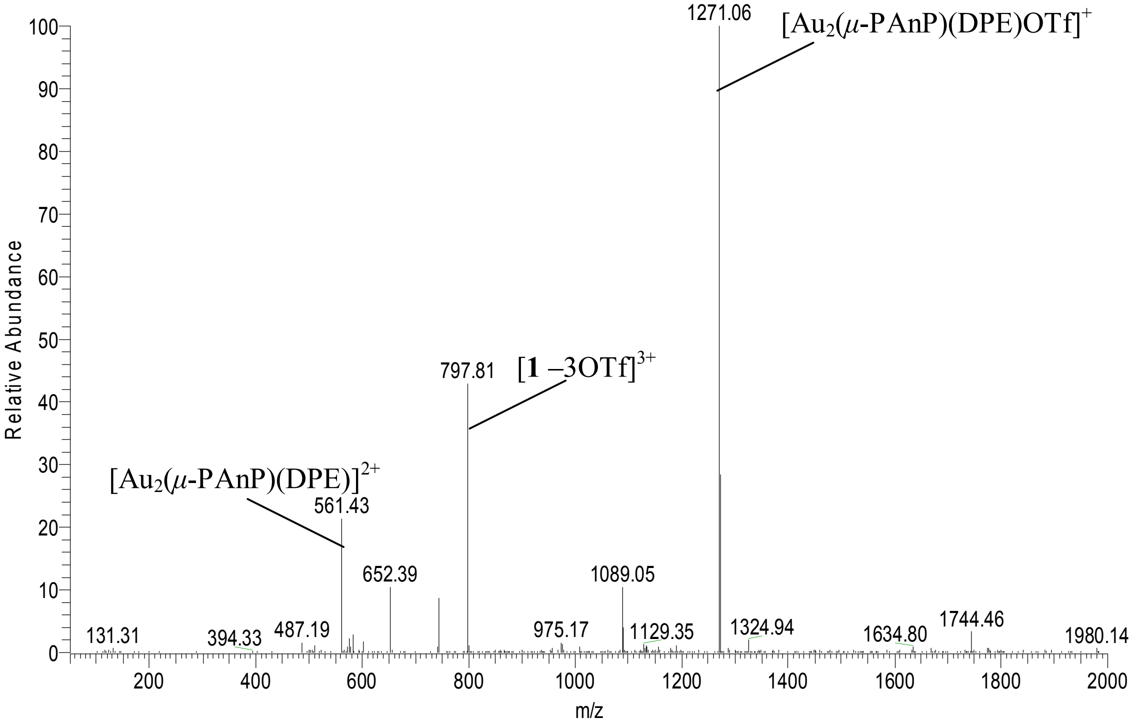

Figure 2.3 ESI-MS of **1**

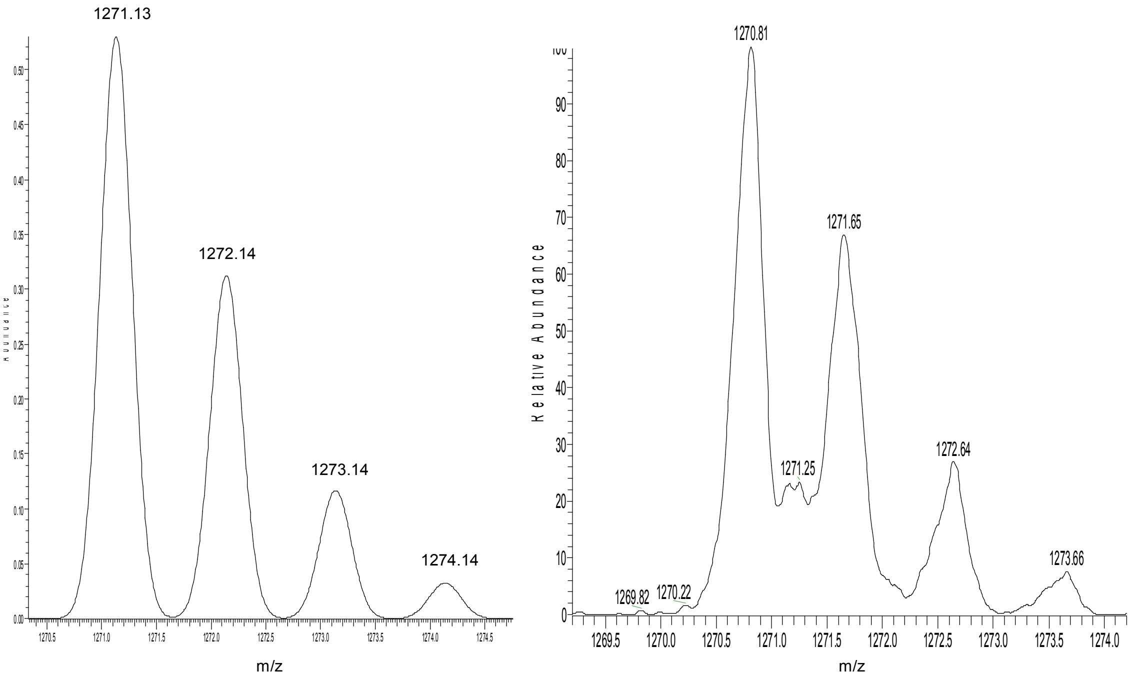

Figure 2.4 Simulated ESI-MS peak for [Au$_2$(μ-PAnP)(DPE)OTf]$^+$ (Left). Experimental ESI-MS peak corresponding to 2 [Au$_2$(μ-PAnP)(DPE)OTf]$^+$ (Right).

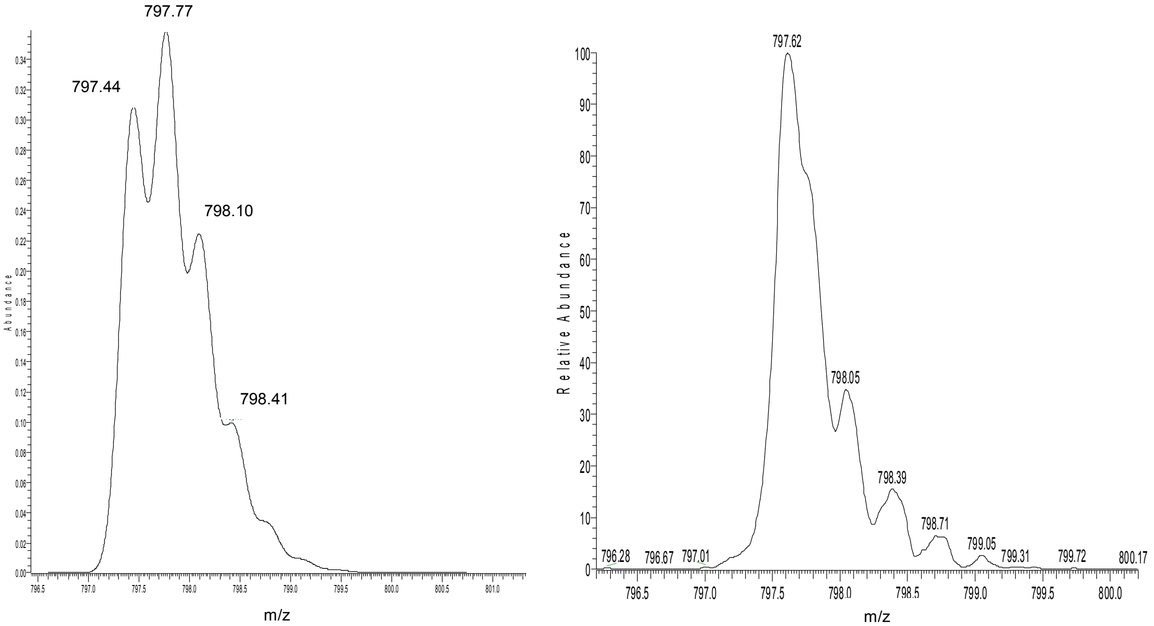

Figure 2.5 Simulated ESI-MS peak for [**1** –3OTf]$^{3+}$ (Left). Experimental ESI-MS peak corresponding to [**1** –3OTf]$^{3+}$ (Right).

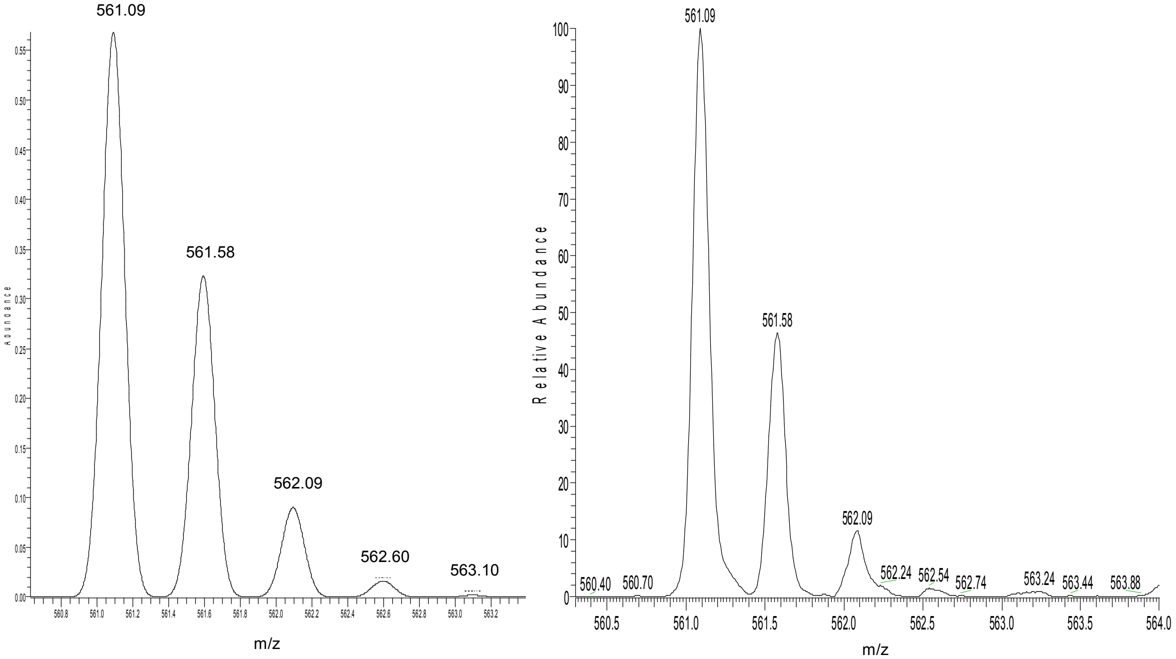

Figure 2.6 Simulated ESI-MS peak for [Au$_2$(μ-PAnP)(DPE)]$^{2+}$ (Left). Experimental ESI-MS peak corresponding to [Au$_2$(μ-PAnP)(DPE)]$^{2+}$ (Right).

2.4.2 X-ray Structural Analysis of 1

Good diffraction quality crystals of **1** were difficult to obtain, as the compounds decomposes readily during crystalization. To overcome this problem, the crystals were grown at low temperature. The crystals were obtained by layering hexane into CH_2Cl_2/MeOH (8:2, v/v) solution of **1** in an NMR tube. The crystal was mounted in capillary for the diffraction experiment to prevent loss of solvent.

The X-ray crystal structure of **1** reveals a tetracation comprising of two opposite $[Au_2(\mu\text{-}PAnP)]^{2+}$ units linked by two DPE ligands (Figures 2.7 and 2.8). The complex displays a rectangular shape being fenced on its four sides by the anthracenyl and pyridyl rings. The complex shows a local C_{2h} symmetry where the C_2 axis bisects the ethylene of the DPE ligand. The center of inversion coincides with the center of the rectangle. Due to the poor diffraction data, the OTf$^-$ anions were difficult to locate. The rectangle contains a large cavity; the distance between the centroids of the opposite anthracenyl rings *X*-*X'* is 19.093 Å. The width of the rectangle, taken as the distance between the ethylene-carbon of the two opposite DPE ligands, is 8.108 Å.

Table 2.1 Selected bond length (Å), angles (deg) of **1**

Au-Au[1]	7.13	Au(1)-P(1)	2.240(2)
P-P[1]	6.46	Au(1)-N(1)	2.058(7)
N-N[1]	7.66	C(13)-P(1)-Au(1)	108.1(2)
γ-C-γ-C[1]	7.95	P(1)-Au(1)-N(1)	175.53(19)
C_{alkene}-C_{alkene}[1]	8.11	Au(1)-N(1)-C(3)	173.8
C(6)-C(7)	1.301(17)		

[1] Intrannular Au-Au, P-P, N-N, γ-C-γ-C and C_{alkene}-C_{alkene} distances.

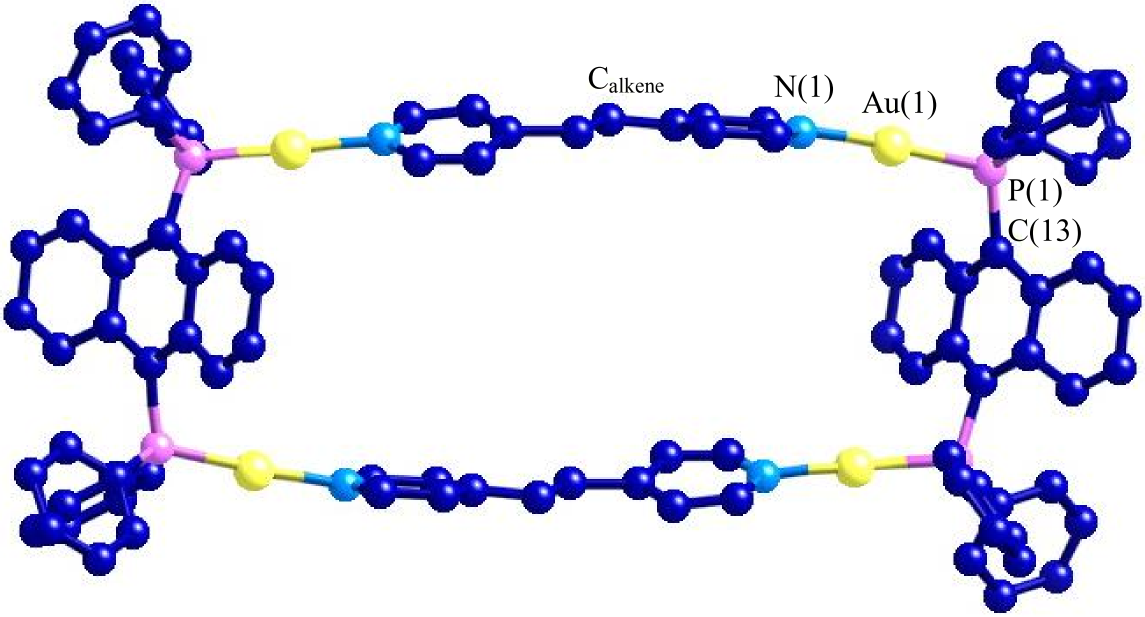

Figure 2.7 Ball and stick representation of the top view of **1**. Hydrogen atoms, anions and solvent molecules are omitted. Color scheme: Au (yellow), N (cyan), P (pink), C (blue)

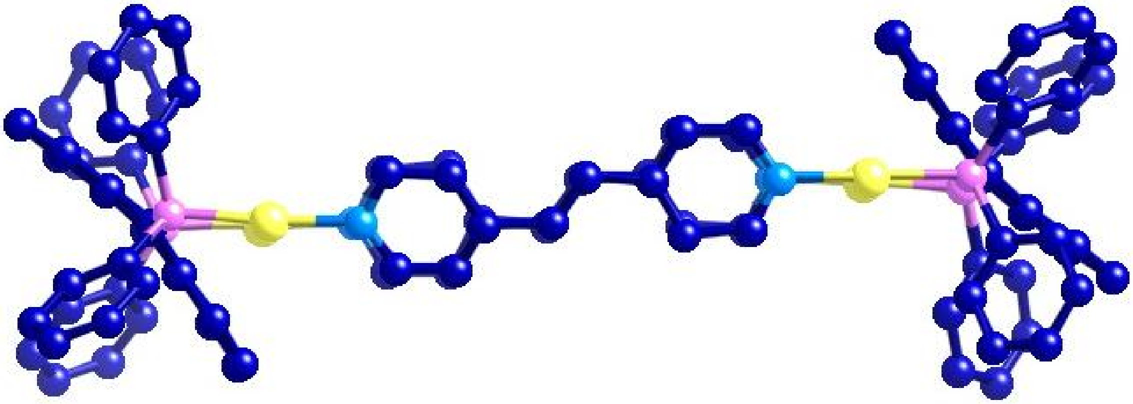

Figure 2.8 Ball and stick representation of the side view of **1**. Hydrogen atoms, anions and solvent molecules are omitted.

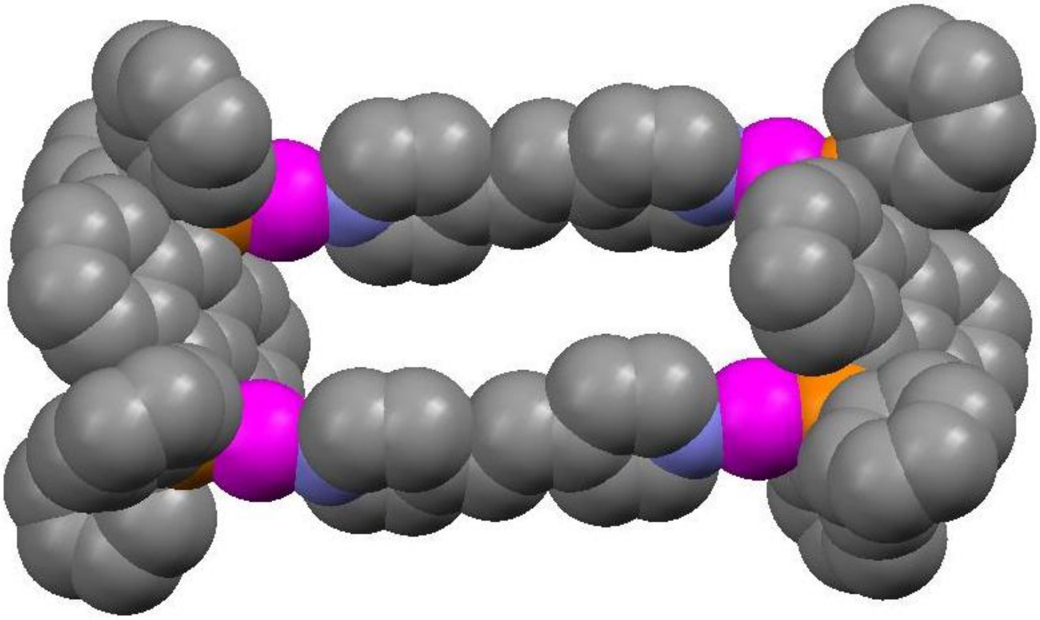

Figure 2.9 Space filling representation of **1**. Hydrogen atoms, anions and solvent molecules are omitted.

The tetracation is slightly bellied on its four sides. The bulging is due to the divergence of the Au-P bonds from the long meridian (C(anthracenyl)-P(1)-Au(1) = 108.1°) and the offset between the central axis of the DPE and the Au-P bond (Au(1)-N(1)-C(3) = 173.8°). The Au-Au distance was drastically shortened from 9.154(2) Å in $Au_2(\mu\text{-}PAnP)(NO_3)_2$ to 7.13 Å in **1**. As the Au centers are now much closer to the anthracenyl rings, the steric repulsion between the metal atoms and peripheral hydrogen atoms of the rings would be much more severe. To alleviate the repulsion, the anthracenyl rings in **1** are curved away from the Au atoms. These conformational changes are possible because of the flexible anthracenyl backbone. The shortening of the Au-Au distance and the bending of the DPE are to maintain the linear metal coordination (P(1)-Au(1)-N(1) = 175.5°) which is the preferred geometry of Au^I ion. The two pyridyl rings of DPE are not coplanar. The internal C(anthracenyl)-P-Au angle of 108.1° is close to a ideal tetrahedral.

The two opposite anthracenyl rings are parallel and tilted towards one end of the rectangle. The eight phenyl rings in **1** can be grouped into two geometrically different sets: four axially-oriented phenyl rings (Ph_{ax}) and four equatorially-oriented phenyl rings (Ph_{eq}). The tilting of the anthracenyl rings could be due to the steric repulsion from the nearly vertical Ph_{ax} rings.

The crystal structure also reveals the intermolecular interaction between the ions along *a*-axis (Figure 2.11). There are π-π interactions between the DPE ligands from adjacent ions. The distance between the two DPE ligands is 3.72Å. Located at the side of two **1** ions are four OTf^- ions.

Viewing down the *a*-axis, one would see one end of the anthracenyl ring pointing towards one of the equatorially-oriented phenyl ring of the neighboring rectangle. This orientation allows complementary edge-to-face interactions between the anthracenyl and Ph_{eq} rings. The H_2 and H_3 of the anthracenyl ring are directed towards the centroid of Ph_{eq} with the calculated H···centroid distances of 3.56 and 4.08 Å (Figure 2.10)

The solid state packing of **1** showed that each ion is surrounded by four neighboring ions (Figure 2.12). The packing led to highly porous crystal with large interstitial space and open channels along the *b*-axis.

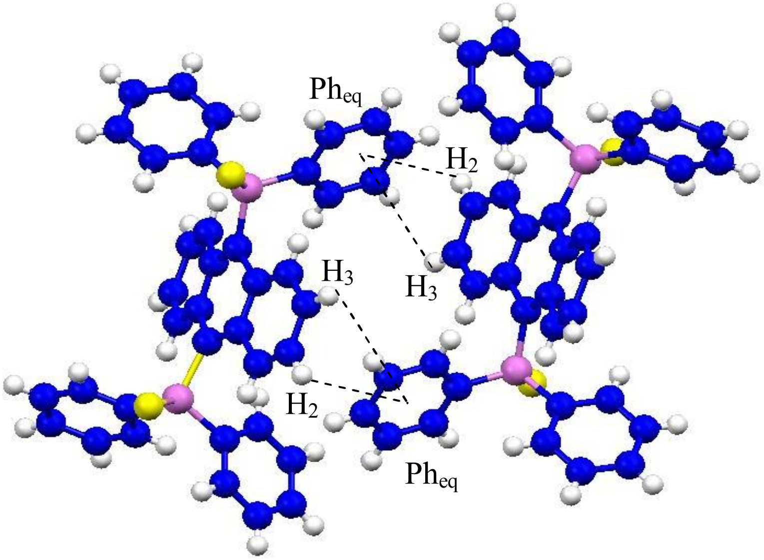

Figure 2.10 Complimentary edge-to-face interactions between the anthracenyl H_2 and H_3 with Ph$_{eq}$ rings. Color scheme: Au (yellow), P (pink), C (blue), H (white)

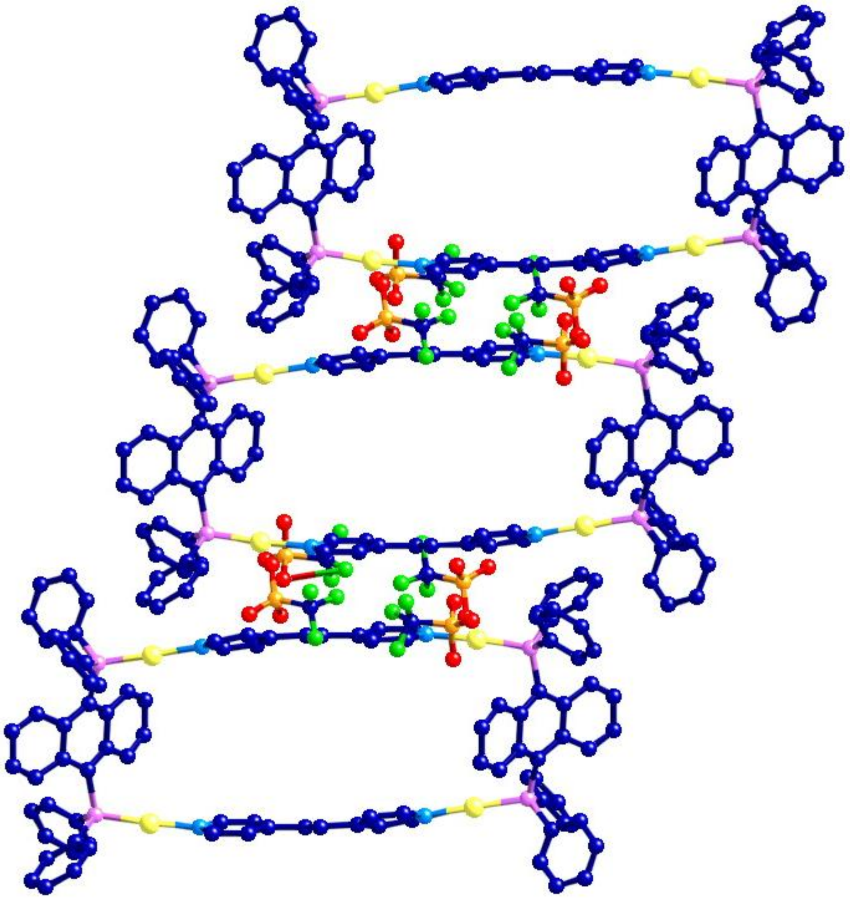

Figure 2.11 Crystal packing diagram of **1** showing the π-π stacking along *a*- axis. Hydrogen atoms are omitted for clarity. Color scheme: see Figure 2.7

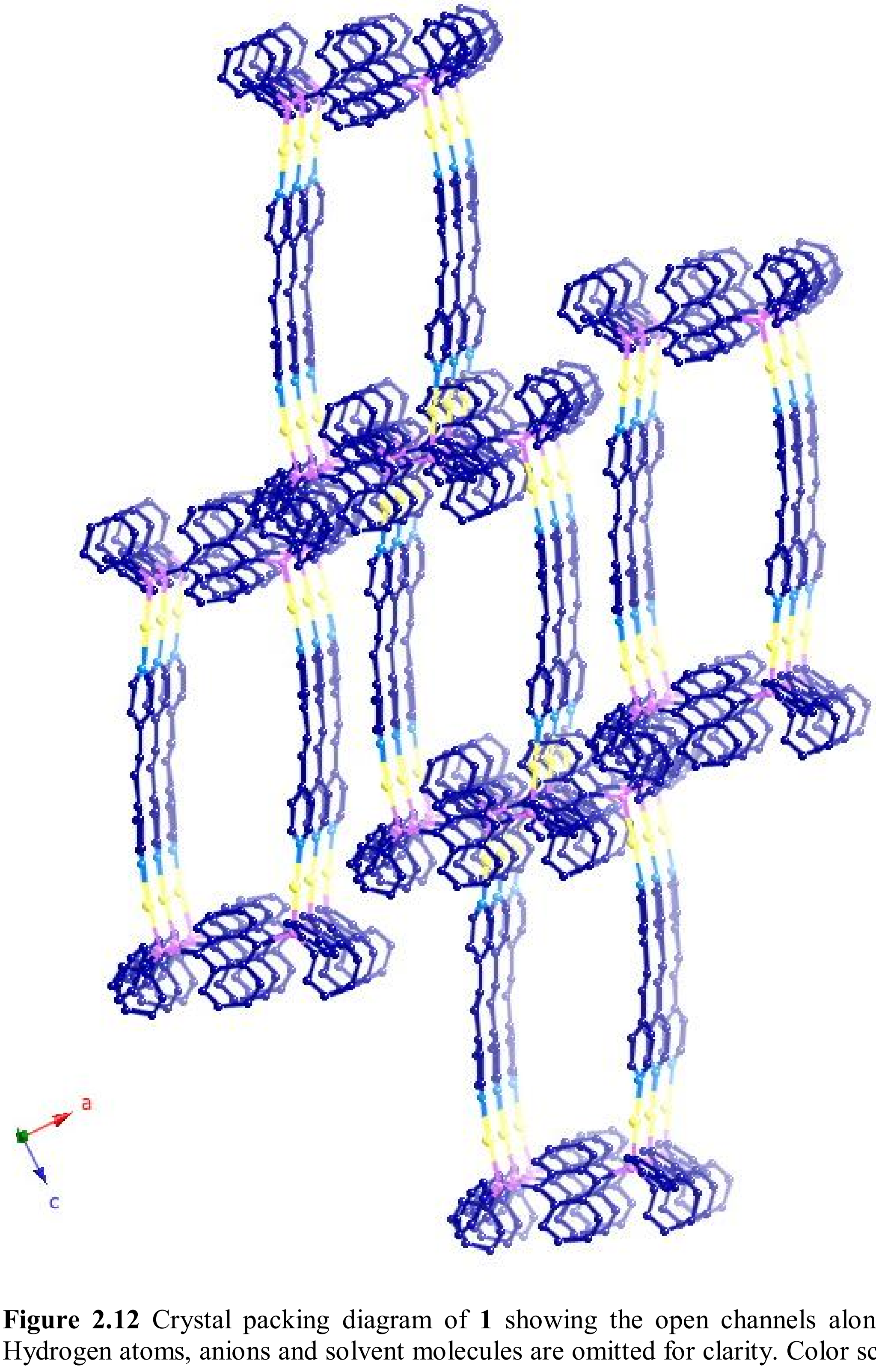

Figure 2.12 Crystal packing diagram of **1** showing the open channels along *b*- axis. Hydrogen atoms, anions and solvent molecules are omitted for clarity. Color scheme: see Figure 2.7

2.4.3 UV-vis Absorption and Luminescence of 1

The UV-vis absorption spectrum of **1** in CH_3CN is shown in the Figure 2.13. The spectrum displays a very intense band at 270 nm (ε_{max} = 1.0x10^5 M^{-1} cm^{-1}) which corresponds to the high energy $^1\pi \rightarrow \pi^*$ transition of the anthracenyl rings. In addition, there is a moderately intense absorption band in 350 - 480 nm which displays vibronic peaks at 392, 420 and 441 nm (λ_{max} = 441 nm, ε_{max} =1.8x10^4 M^{-1} cm^{-1}). The band at 304 nm (ε_{max} = 6.3x10^4 M^{-1} cm^{-1}) is due to the $^1\pi \rightarrow \pi^*$ transition of the DPE ligands. It is slightly red shifted as compared to the free DPE molecules.

Irradiating a solution of **1** at 420 nm gives an emission maximized at 480 nm with quantum yield of 10^{-3} (Figure 2.14). The small Stokes shift indicates that the emission is $^1\pi \rightarrow \pi^*$ fluorescence.

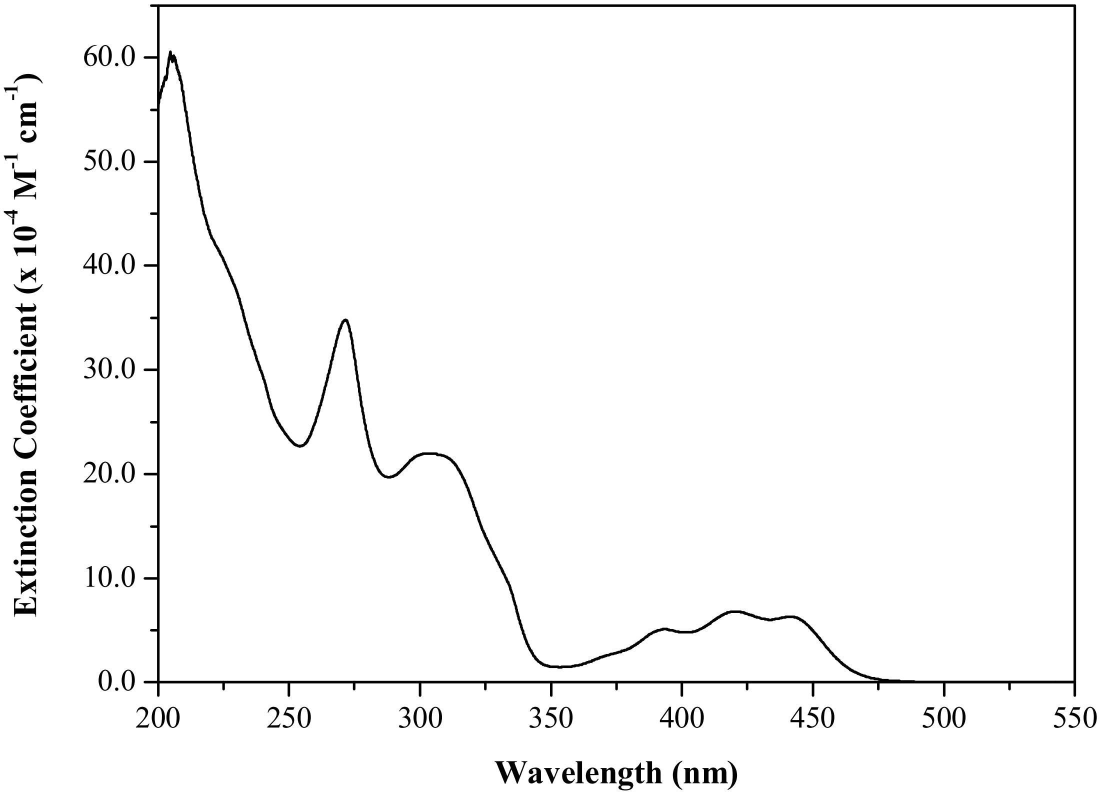

Figure 2.13 UV-vis absorption spectrum of **1** in CH_3CN, T = 298 K.

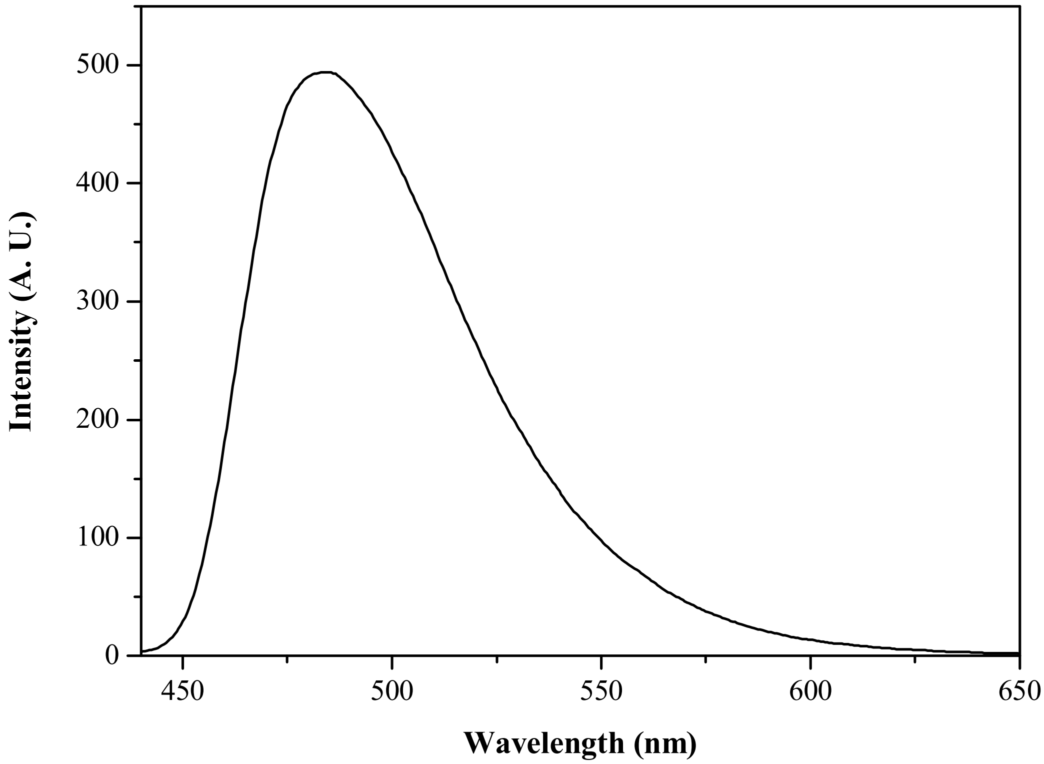

Figure 2.14 Emission spectra of **1** in CH_3CN, T = 298 K. Excitation wavelength = 420nm, excitation and emission slit widths = 10 nm.

2.4.4 Structure of $[Au_4(\mu\text{-PAnP})_2(\mu\text{-BPE})_2](OTf)_4$ 2

The synthesis of **2** followed the same reaction as **1** but the ligand was changed to 1,2-bis(4-pyridyl)ethane and the reaction was carried out in CH_2Cl_2 instead of CH_2Cl_2/MeOH mixture. Unlike **1** which is sparingly soluble in CH_2Cl_2, **2** is very soluble in CH_2Cl_2 and CH_3CN. A longer reaction time was required to form the gold rectangle probably because of the ligand being less rigid than the DPE.

The $^{31}P\{^1H\}$ NMR spectrum of **2** (Figure 2.15) was recorded in $CDCl_3$ and is similar to that of **1**. There is a sharp singlet at 21.80 ppm, which suggests the formation of a discrete and highly symmetric complex.

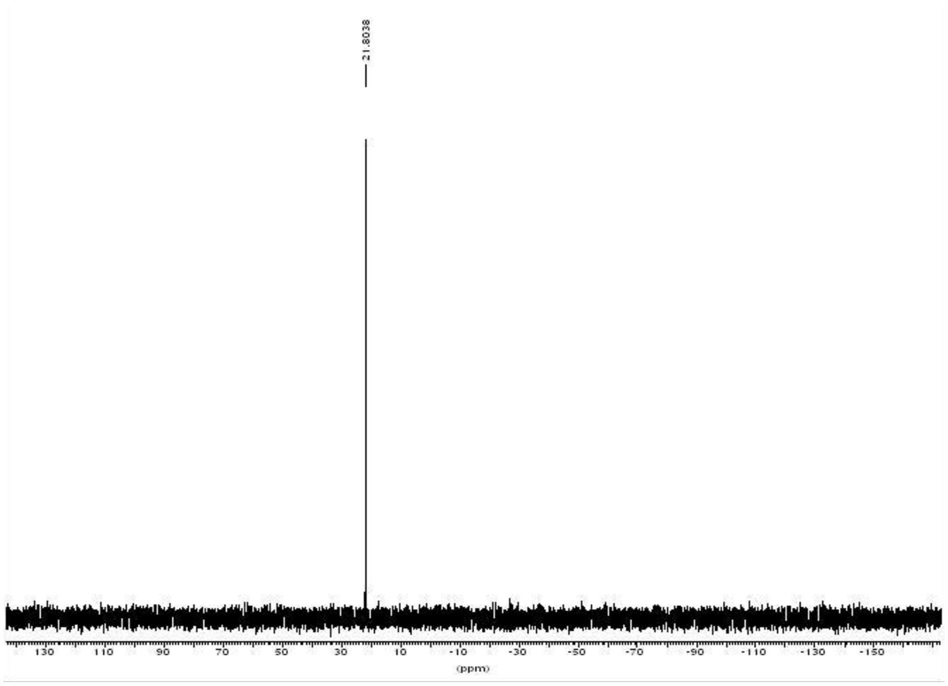

Figure 2.15 $^{31}P\{^{1}H\}$ NMR spectrum of **2** (300 MHz, $CDCl_3$)

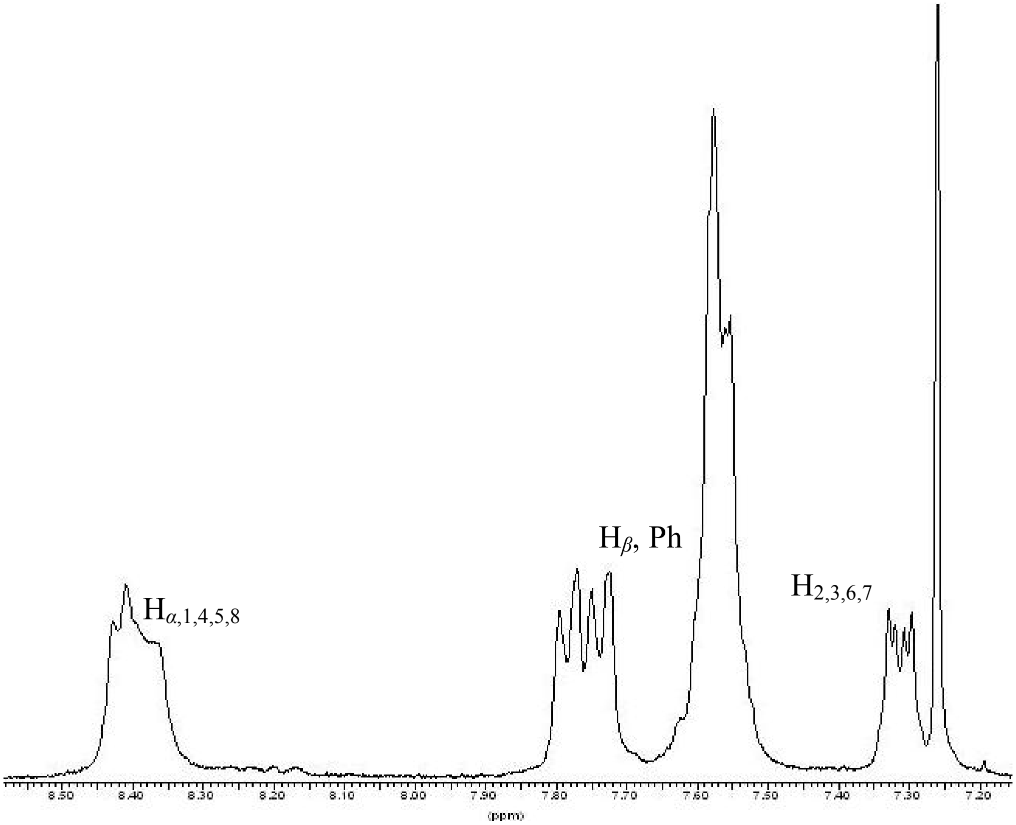

Figure 2.16 ^{1}H NMR spectrum of **2** (300 MHz, $CDCl_3$)

In the ^{1}H NMR spectrum of **2**, the doublet for the α-protons merges with the multiplets due to the protons in the meso position in the anthracenyl ring to form a peak in the δ 8.30 - 8.50 (Figure 2.16). The peaks in the δ 7.50 - 7.80 are attributed to the protons in the phenyl rings and the β-protons of the pyridyl rings. The peak at δ 7.33 is due to the $H_{2,3,6,7}$ of the anthracenyl ring.

The ESI-MS spectrum of **2** showed four charged peaks at m/z = 1272.97, 1008.17, 798.70 and 562.37 (Figure 2.17). The peak at m/z = 798.70 is attribute to the molecular ion $[\mathbf{2} - 3OTf]^{3+}$. The most prominent peak at m/z 1272.97 belongs to the "half-rectangle" $[Au_2(\mu\text{-}PAnP)(BPE)OTf]^+$. Another peak at m/z 561.43 can also be attributed to the ion $[Au_2(\mu\text{-}PAnP)(BPE)]^{2+}$. There is a peak at m/z = 1008.17 which can be attributed to the ion $[Au_2(\mu\text{-}PAnP)OTf]^+$. The assignments are further confirmed by simulated isotopic distributions (Figures 2.18 - 2.20). These results lend support to the rectangular structure of **2**. Elemental analysis of the compound also agrees well with the proposed molecular formula.

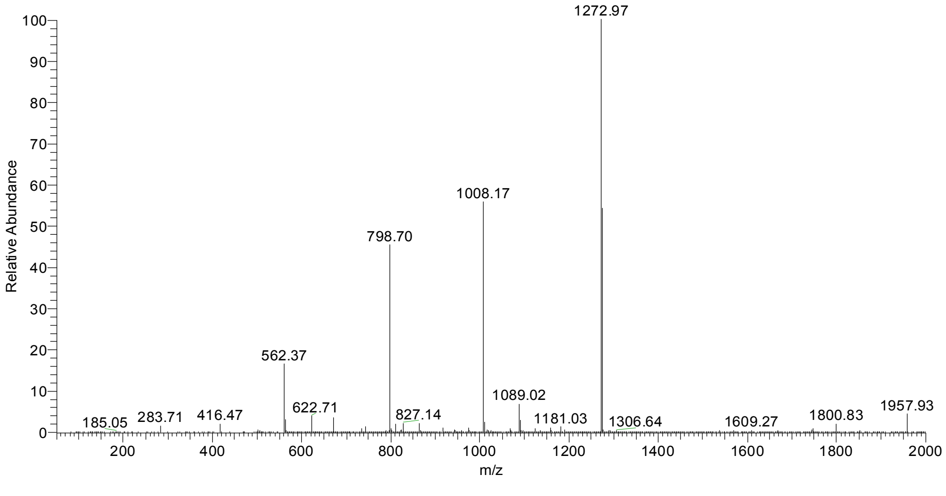

Figure 2.17 ESI-MS of **2**

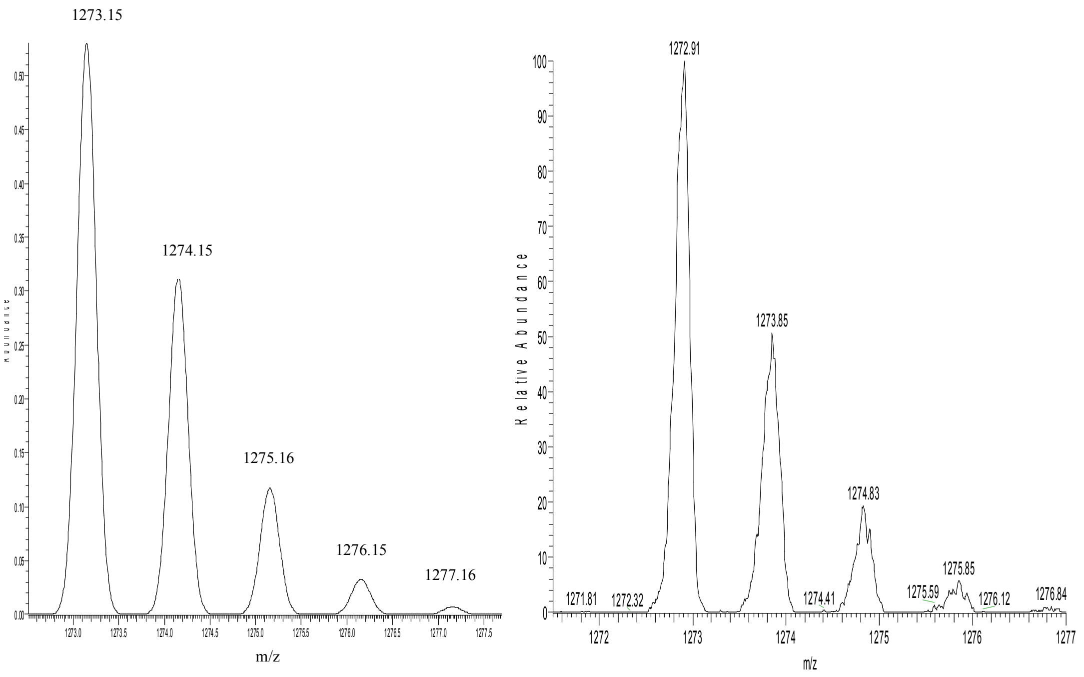

Figure 2.18 Simulated ESI-MS peak for [Au_2(μ-PAnP)(BPE)OTf]$^+$ (Left). Experimental ESI-MS peak corresponding to 2 [Au_2(μ-PAnP)(BPE)OTf]$^+$ (Right).

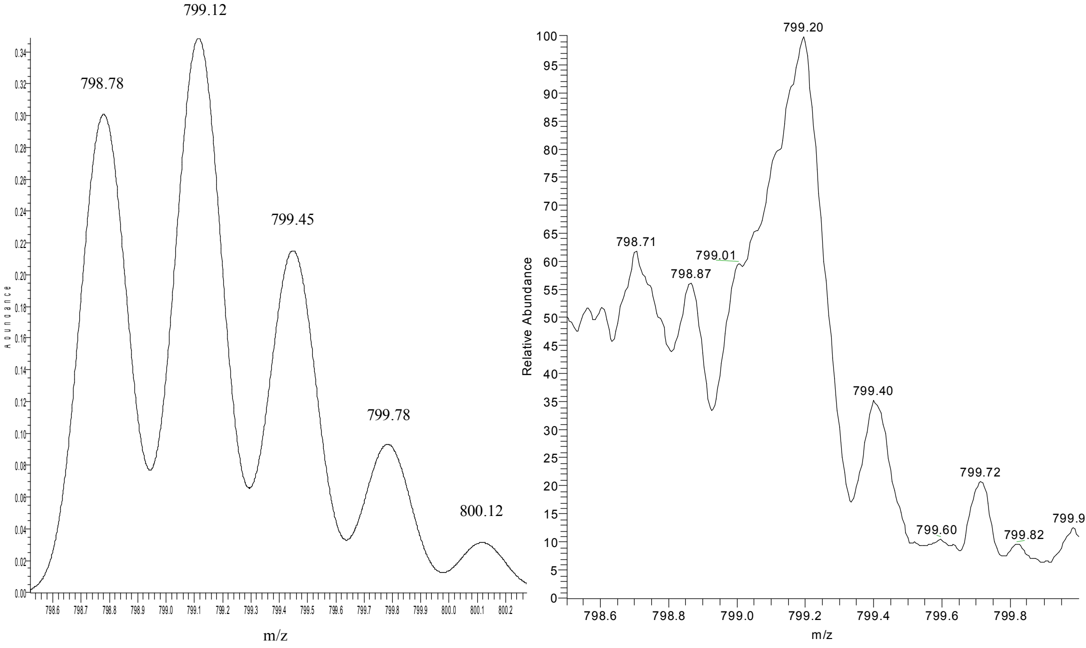

Figure 2.19 Simulated ESI-MS peak for [**2** –3OTf]$^{3+}$ (Left). Experimental ESI-MS peak corresponding to [**2** –3OTf]$^{3+}$ (Right).

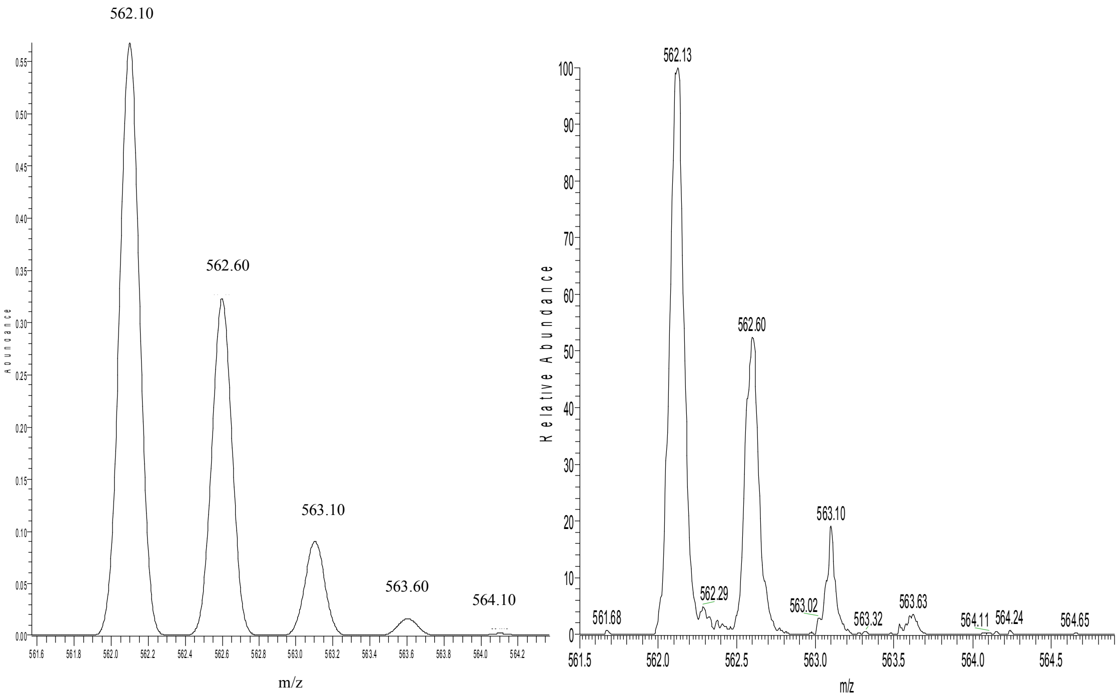

Figure 2.20 Simulated ESI-MS peak for $[Au_2(\mu\text{-PAnP})(BPE)]^{2+}$ (Left). Experimental ESI-MS peak corresponding to 2 $[Au_2(\mu\text{-PAnP})(BPE)]^{2+}$ (Right).

2.4.5 X-ray Structural Analysis of 2

Good diffraction quality crystals of **2** were difficult to obtain. Similar to **1**, the crystals of **2** lose solvent readily. The crystals were obtained by layering iso-octane into CH_2Cl_2 solution of **2** in an NMR tube. The crystal data obtained for **2** was poor. Nevertheless, the structural feature of the tetracation can still be confirmed. The X-ray crystal structure reveals two $[Au_2(\mu\text{-PAnP})]^{2+}$ units connected to two BPE ligands (Figures 2.21 and 2.22). The BPE ligands are disordered as they are highly flexible and the two BPE ligands are nearly perpendicular to each other. The cavity of the gold rectangle was 9.197 x 18.662 Å. The anion and solvent molecules were difficult to locate. Two of the C(anthracenyl)-P(1)-Au(1) angles (109.82°) were almost perfert tetrahedral, while the other two (C(anthracenyl)-P(2)-Au(2) = 111.41°) were slightly bigger. All the N-Au-P (167.08° - 178.23°) angles are close to the ideal linear metal coordination geometry which is preferred by Au^I ions, except one angle (N(1)-Au(1)-P(1) = 167.08º) which is slightly smaller.

The crystal is in orthorhombic space group, Pbam. In Figure 2.23, the crystal packing reveals rows of gold rectangles with spaces between each row along the *a*-*b* plane. There are no open channels as seen in the packing of **1**.

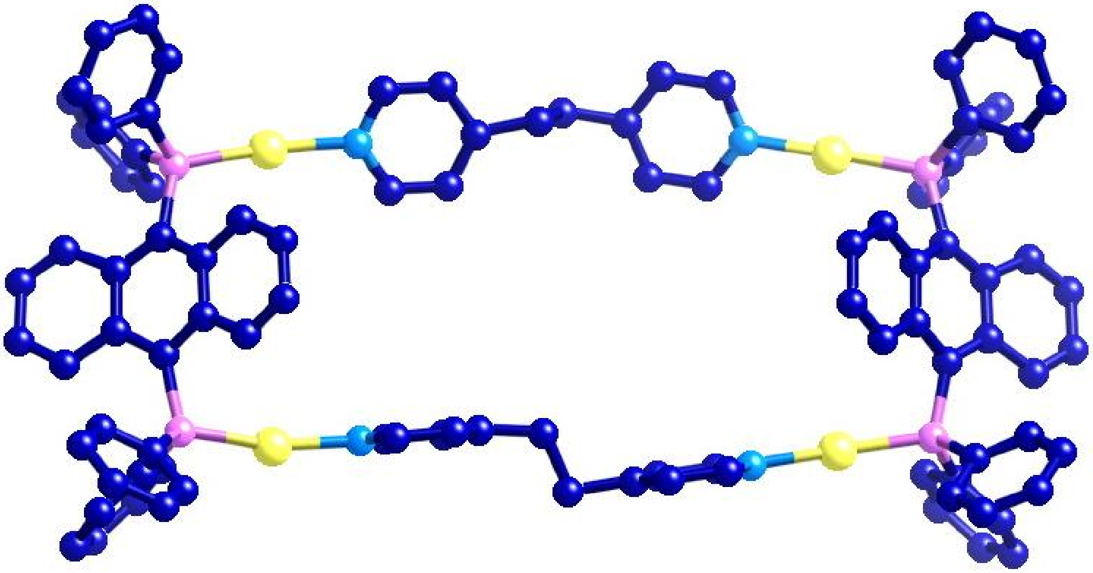

Figure 2.21 Ball and stick representation of the top view of **2**. Hydrogen atoms, anions, solvent molecules and disorder are omitted. Color scheme: Au (yellow), N (cyan), P (pink), C (blue)

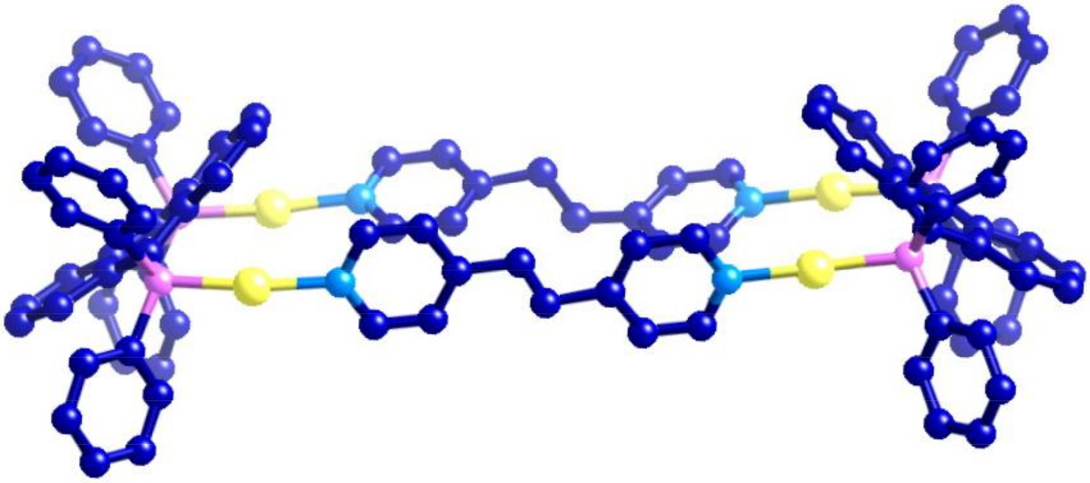

Figure 2.22 Ball and stick representation of the side view of **2**. Hydrogen atoms, anions, solvent molecules and disorder are omitted.

Table 2.2 Selected bond length (Å), angles (deg) of **2**

Au-Au[1]	7.126	N(1)-Au(1)-P(1)	167.08
P-P[1]	6.414	N(2)-Au(2)-P(2)	171.30
N-N[1]	7.881	N(1XA)-Au(1A)-P(1A)	178.23
C_{alkane}-C_{alkane}[1]	9.197	N(2XA)-Au(2A)-P(2A)	174.13
C(8)-P(1)-Au(1)	109.82	C(1)-P(2)-Au(2)	111.41

[1] Intrannular Au-Au, P-P, N-N and C_{alkane}-C_{alkane} distances.

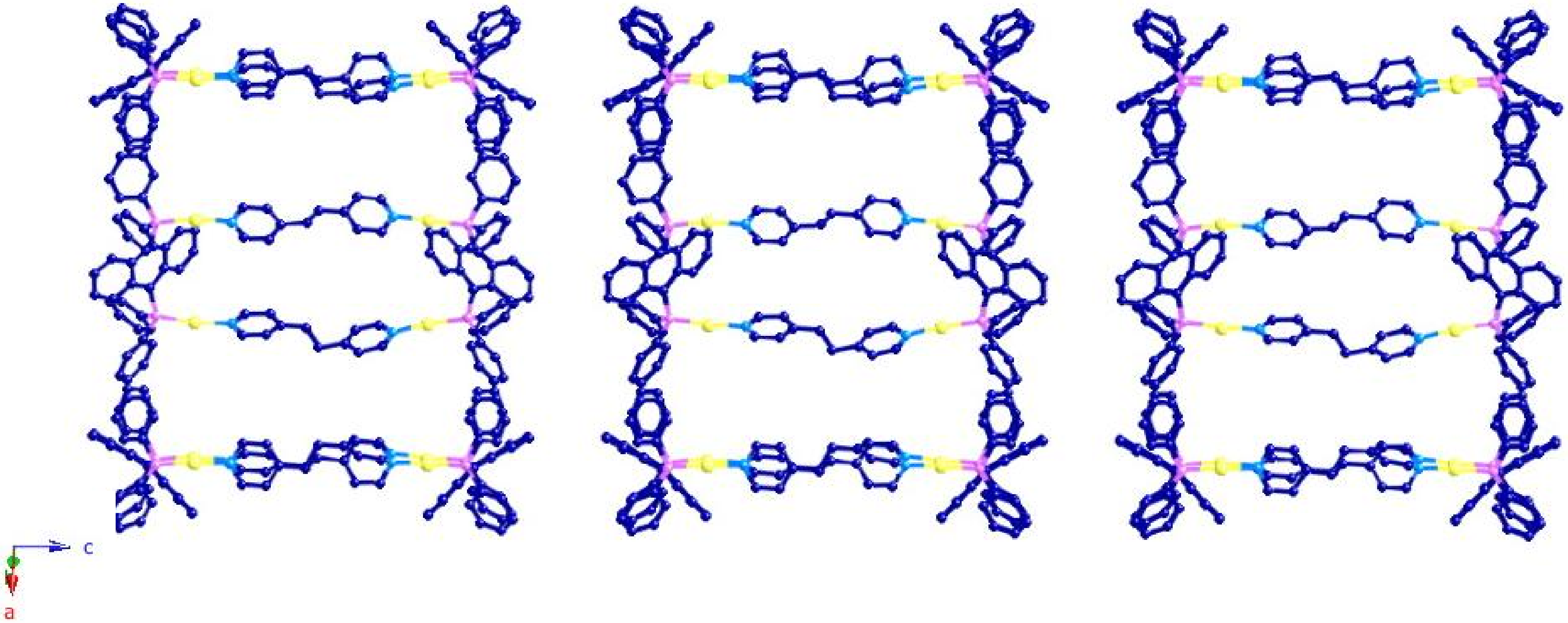

Figure 2.23 Crystal packing diagram of **2** along *c*-axis. Hydrogen atoms, disordered anions, solvent molecules and disorder are omitted for clarity. Color scheme: see Figure 2.21

2.4.6 UV-vis Absorption and Luminescence of 2

The UV-vis absorption spectrum of **2** in CH_3CN as shown in Figure 2.24 is similar to that of **1**. The very intense band at 270 nm (ε_{max} = 6.8x10^4 M^{-1} cm^{-1}) corresponds to the high energy $^1\pi \rightarrow \pi^*$ transition of the anthracenyl rings. The moderately intense absorption band in 350 - 480 nm displays vibronic peaks at 393, 420 and 443 nm (λ_{max} = 443 nm, ε_{max} =1.6x10^4 M^{-1} cm^{-1}).

Irradiating a solution of **2** at 420 nm gives an emission maximized at 480 nm with quantum yield of 0.048 (Figure 2.25). The small Stokes shift indicates that the emission is $^1\pi \rightarrow \pi^*$ fluorescence.

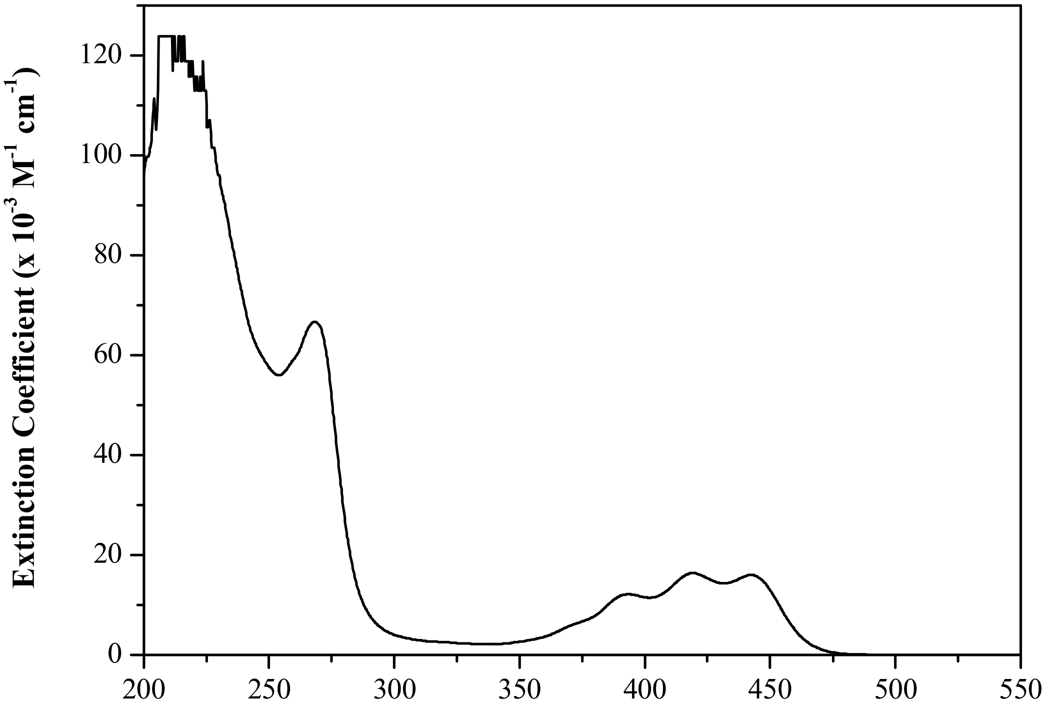

Figure 2.24 UV-vis absorption spectrum of **2** in CH_3CN, T = 298 K

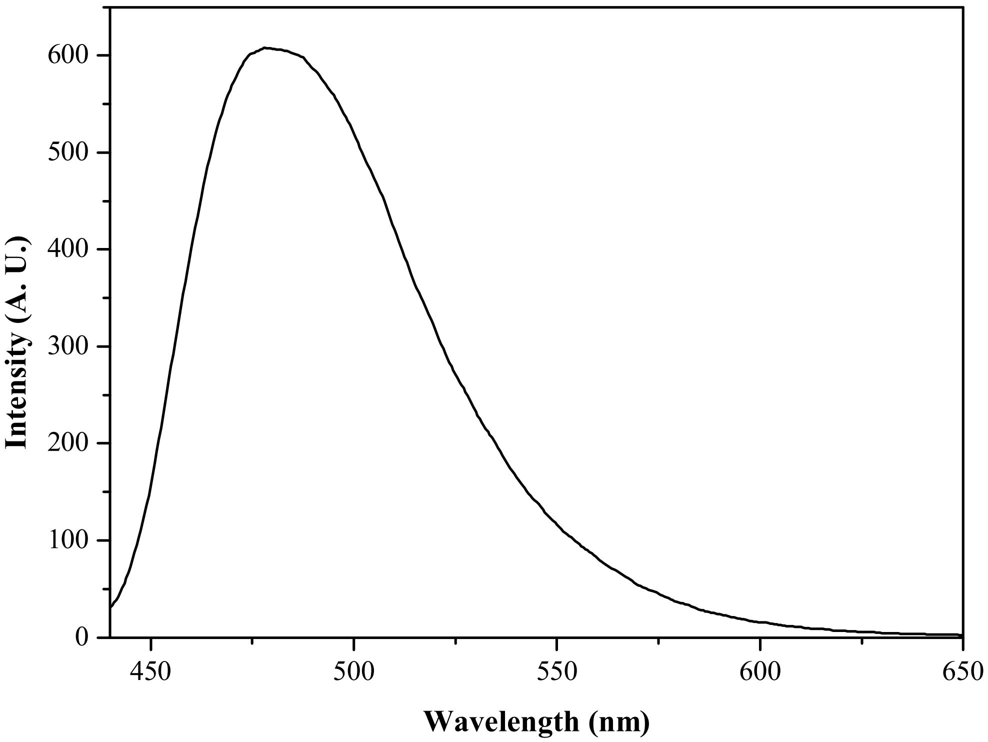

Figure 2.25 Emission spectrum of **2** in CH_3CN, T = 298 K. Excitation wavelength = 420 nm, excitation and emission slit widths = 10 nm.

2.5 Fluorescence Quenching of Host

The complexations between the gold rectangles and the aromatic guests were investigated by fluorescence titration. The emissions of **1** and **2** at 480 nm are quenched by anthrence (An), bromoanthrence (Br-An), napthlene (Nap) and pyrene (Py) (Figure 2.26). Figure 2.27 shows the change of the emission intensity of **1** upon addition of An. Since all the guests virtually have no absorption beyond 460 nm, the decrease is not due to the internal absorption of the guests. Titration curves are obtained by plotting the intensity I_H against $[G]_t$ (I_H is the emission intensity of **1** in the presence of the guest). The binding constants K_Q for the guests were determined from the least square fit to the equation 1 for 1:1 host-guest complexation (Figures A1-6).

$$I_H = I_H^{\circ} - [\frac{\Delta I_H}{2[H]_t}(B - \sqrt{B^2 - 4[H]_t[G]_t})] \qquad \text{eq. 1}$$

$$B = [H]_t + [G]_t + \frac{1}{K_Q} \qquad \text{eq. 1.1}$$

Figure 2.28 shows the titration curve for fluorescence intensity of **1** upon addition of An to a CH_3CN solution of the compound. The binding constant, K_Q and the binding free energy, $-\Delta G_Q$ for both gold rectangles are listed in **Table 2.3**. The binding constants were very low, with the exception of the binding constant with pyrene which was slightly higher. The low binding constant was due to the mismatch in the size of the cavity and that of the aromatic guests. Nap being the smallest among all the aromatic guests has the lowest binding constants with both gold rectangles. On the other hand, Py is bigger and has a higher binding constant.

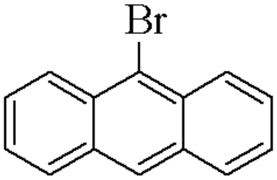

9- bromoanthracene
Br-An

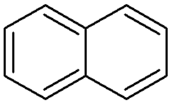

napthalene
Nap

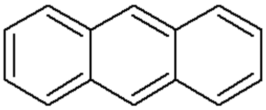

anthracene

An

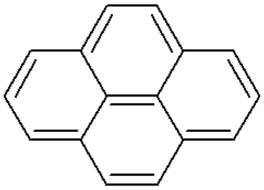

pyrene

Py

Figure 2.26 Structures of aromatic guests

The binding constant of Py with **2** could not be determined because of the low solubility of Py in a CH_3CN solution of **2**. The large cavities of the gold rectangles present the possibility of hosting larger guest molecules. Host-guest complexation experiments with other aromatic guests are currently being carried out.

Table 2.3 Binding constants and free energy of binding for the aromatic guest determined by fluorescence titrations

	1		**2**	
Guest	K_Q (M^{-1})	$-\Delta G_Q$ (kJ mol^{-1})	K_Q (M^{-1})	$-\Delta G_Q$ (kJ mol^{-1})
An	63 ± 9	10.5 ± 0.71	37 ± 3	8.9 ± 0.40
Br-An	79 ± 1	10.8 ± 0.06	36 ± 7	8.8 ± 0.97
Nap	49 ± 2	9.6 ± 0.02	12 ± 2	6.2 ± 0.83
Py	158 ± 8	12.5 ± 0.25	a	

[a]cannot be determined

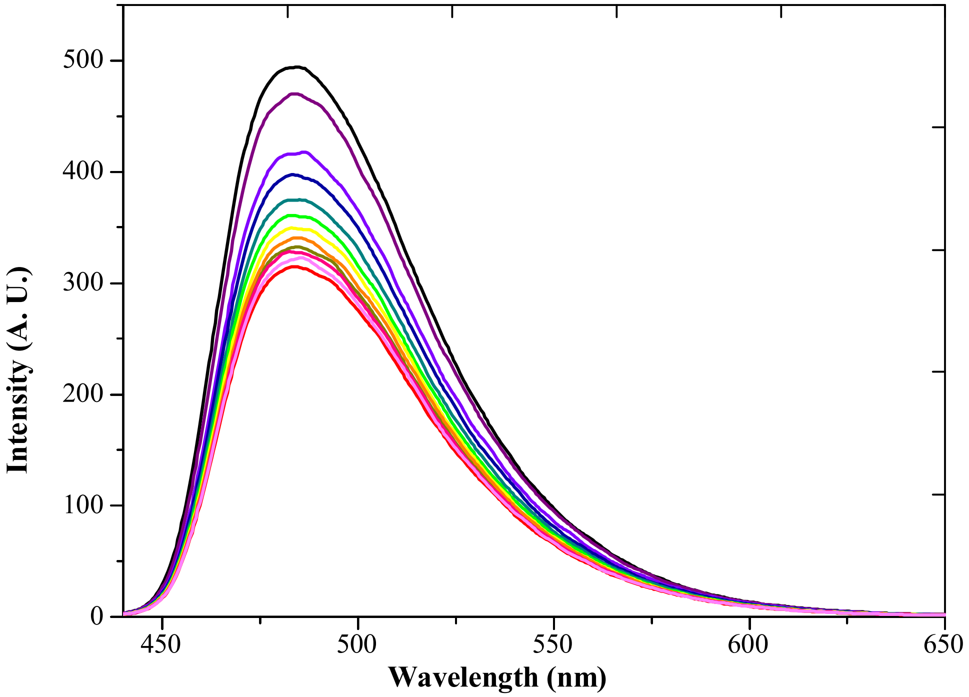

Figure 2.27 Emission spectral change upon addition of An to a CH_3CN solution of **1**. Excitation wavelength = 420 nm, excitation and emission slit width = 10 nm.

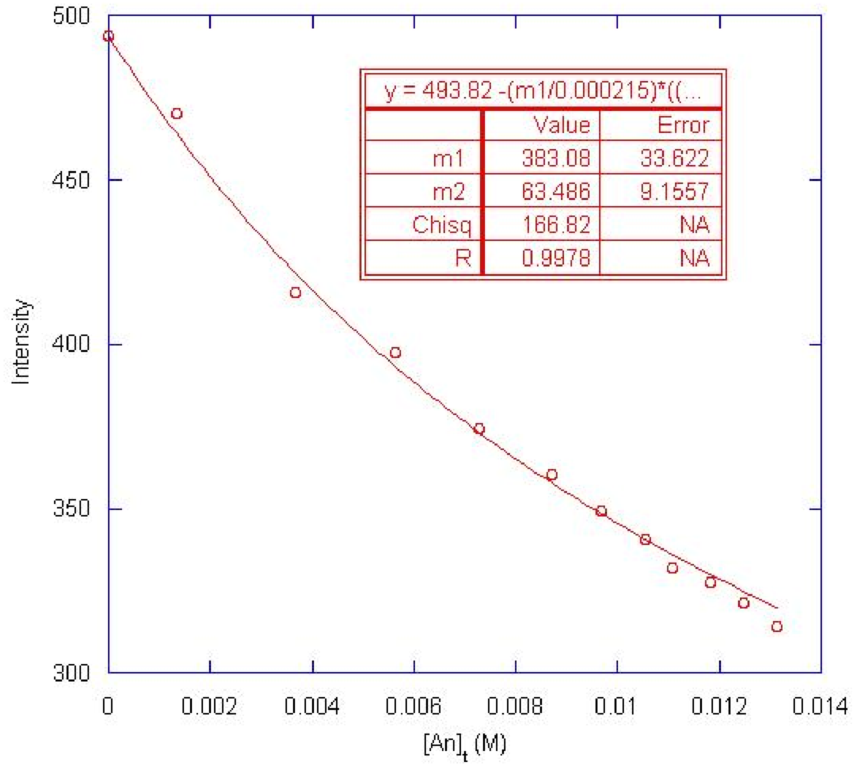

	Value	Error
m1	383.08	33.622
m2	63.486	9.1557
Chisq	166.82	NA
R	0.9978	NA

Figure 2.28 Emission titration curve upon addition of An to a CH_3CN solution of **1.** Line shown is the least square fit using equation 1.

2.6 Conclusion

In this chapter, we have demonstrated the facile synthesis of two Au^I molecular rectangles, $[Au_4(\mu\text{-PAnP})_2(\mu\text{-DPE})_2](OTf)_4$ and $[Au_4(\mu\text{-PAnP})_2(\mu\text{-BPE})_2](OTf)_4$ by the self-assembly between the molecular "clip" $Au_2(\mu\text{-PAnP})Cl_2$ and the DPE and BPE ligands respectively. Their synthesis took place via a one-pot reaction and was synthesized in high yield. The crystal packing of $[Au_4(\mu\text{-PAnP})_2(\mu\text{-DPE})_2](OTf)_4$, **1** shows a open channel along *b*-axis and π-π stacking of the DPE ligands along *a*-axis. There are also complementary edge-to-face Ph-Ph interactions between the phenyl ring and anthracenyl backbone.

The crystal packing of $[Au_4(\mu\text{-PAnP})_2(\mu\text{-BPE})_2](OTf)_4$, **2** did not have the open channel as seen in **1**. The gold rectangles were arranged in rows along the *a*-*b* plane.

Both Au^I molecular rectangles are receptor for aromatic molecules of different sizes and electronic properties. The fluorescence of the Au^I rectangles was quenched upon guest binding. The binding constants were low due to the large cavity of the rectangles and the small size of the aromatic guest.

CHAPTER 3

SURFACE TECHNIQUES AND CHARACTERIZATION

3.1 Introduction

Self-organized molecular layers provide a promising route to constructing new nanodevices and optimizing nannosensors.[63, 64, 66, 102, 103] One approach towards this goal is to examine the molecular layers with scanning probe microscopy.

Recently, Gong et al have described experiments using highly ordered pyrolytic graphite (HOPG) and Cu(100) surfaces for the deposition of supramolecular squares and rectangles.[76] The complexes deposit in a flat orientation and open their cavity toward the solution phase. Scanning probe microscopy such as scanning tunneling microscopy (STM) and atomic force microscopy (AFM) is a powerful tool for characterizing surface structure. The self-assembly and self-organization of a wide range of organic molecules have been studied by STM.[104, 105] However, only recently has scanning probe techniques been used to study supramolecular molecules on surfaces.[77] One future goal is to use this arrangement of supramolecular macrocycles for a surface confined host-guest chemistry that can be directly visualized by means of STM. $[Au_4(\mu\text{-PAnP})_2(\mu\text{-bipy})_2](OTf)_4$ was used in the formation of SAM because of its stability.

Other surface techniques such as X-ray photoelectron spectroscopy (XPS) and ellipsometry are used to characterize the molecular layers.[83] It gives information on the chemical states of the atoms and layer thickness. In the following section, brief theory on the principles of XPS, ellipsometry and STM are described.

3.2 Theory

3.2.1 X-ray photoelectron spectroscopy (XPS)

XPS, also known by the acronym ESCA (electron spectroscopy for chemical analysis) is a useful technique to yield information of surfaces. Information on the elemental composition and oxidation states of the elements are easily acquired.

XPS is based on the photoelectric effect, in which an atom absorbs a photon of energy hv and a core electron with binding energy E_B is ejected with kinetic energy. The energy of the emitted photoelectrons is then analyzed by the electron spectrometer and the data presented as a graph of intensity (expressed as counts per seconds) versus binding energy. The kinetic energy (E_K) of the electron is the experimental quantity measured by the spectrometer, but this is dependent on the photon energy of the X-rays employed and is therefore not an intrinsic material property. The binding energy of the electron is the parameter which identifies the electron specifically, both in terms of its parent element and atomic energy level. The relationship between the parameters involved in the XPS experiment is:

$$E_B = hv - E_K - W \qquad \text{eq. 2}$$

where W is the spectrometer work function.

As all the three quantities on the right-hand side of the equation are known and or measureable, the binding energy of the electron can be obtained easily.

The process of photoemission is shown schematically in Figure 3.1, where an electron from the K shell is ejected from the atom.

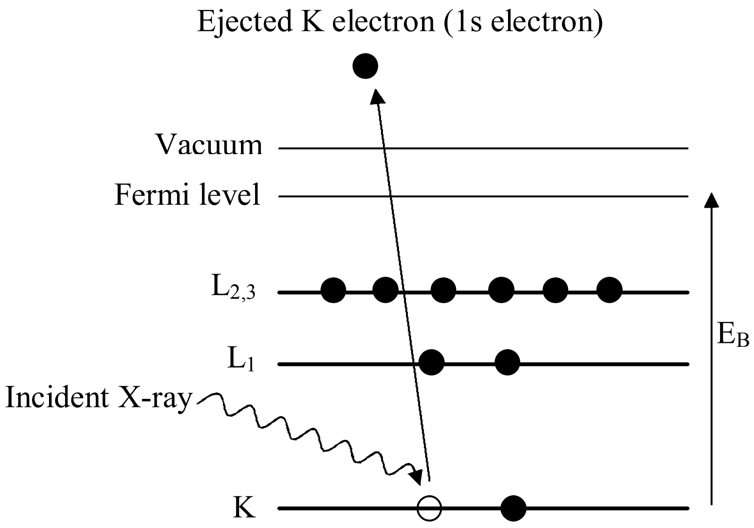

Figure 3.1 Schematic diagram of the XPS process, showing photoionization of an atom by the ejection of a 1s electron.

Those electrons which are excited and escape without energy loss contribute to the characteristic peaks in the spectrum, whereas those which undergo inelastic scattering and suffer energy loss contribute to the background of the spectrum. In addition to the expected peaks, the spectrum also contains peaks due to Auger electrons.

Photoelectron peaks are labeled according to the quantum numbers of the level from which the electron originates. For each level with orbital momentum $l \geq 1$ has two sublevels, with an energy difference called the spin-orbit coupling. For example, Au 4f level gives two photoemission peaks, $4f_{7/2}$ and $4f_{5/2}$

Binding energies are not only element specific but contain chemical information as well. This is because the energy levels of core electrons depend slightly on the chemical state of the atom. Chemical shifts are typically in the range of 0 – 3 eV. In general, the binding energy increases with increasing oxidation state and the electronegativity of the ligands.[106, 107]

3.2.2 Ellipsometry

Ellipsometry is an old technique but it is constantly adapted and made more user friendly with the availability of computers. It is an ideal technique for measuring optical constant as well as film thickness because of their well-known sensitivity to detect a few angstroms change in material layers.[108, 109] Its theory is briefly discussed here.

The basic instrumentation of ellipsometry consists of the following: a monochromatic light source, an optical element to covert unpolarized light to linearly polarized light (polarizer), an optical element that converts linearly polarized light into elliptically polarized light (quarter-wave plate), the sample of interest, an optical element to determine the state of polarization of the resultant light beam (analyzer), a detector to measure the light intensity and calculation facilities to interpret the results. A simple layout of the ellipsometer is shown in Figure 3.2.[110]

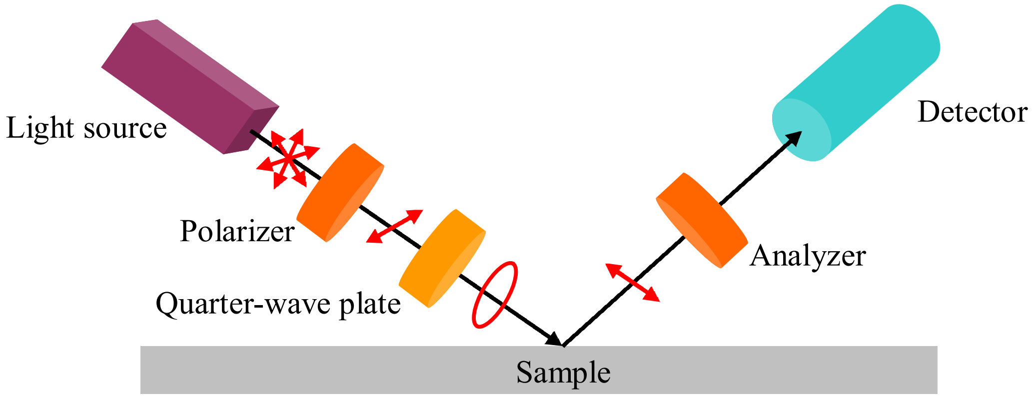

Figure 3.2 Schematic diagram of the layout of an ellipsometer

All thin films are assumed to be perfect, isotropic, and uniform, exhibiting completely smooth and parallel surfaces. The ambient surrounding has no absorption and the substrate is considered to be a thick film that has no interference effects. Ellipsometry measures the change in polarization state of light reflected from the surface of a sample in terms of Ψ (amplitude ratio) and Δ (phase difference), which are related to the ratio of Fresnel reflection coefficients, R_p and R_s for p- and s-polarized light respectively.[111] After a measurement is made, a model is constructed to describe the sample. Figure 3.3 shows a model of the thin film sample with its optical parameters, reflective index (*n*), extinction coefficient (*k*) and film thickness (*d*).

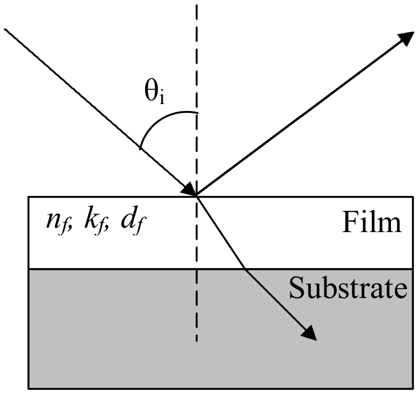

Figure 3.3 Model of thin film sample showing geometry of measurement and the reflected and tranmitted beams.

The model is used to calculate the theoretical data from Fresnel's equations which describe each material with thickness and optical constants. If these values are not known, an estimate will be given for the purpose of the preliminary calculation. These calculated values will be compared to the experimental data. The unknown parameters can be varied to improve the fitting between the experimental and calculated values. However, one should note that the number of unknown properties should not exceed the amount of information contained in the experimental data. For example, a single-wavelength ellipsometer produces two data points (Ψ,Δ) and only a maximum of two parameters are to be determined. Finding the best match between the model and the experiment is typically achieved through regression. An estimator, like the Mean Squared Error (MSE), is used to quantify the difference between curves.

3.2.3 Scanning Tunneling Microscopy (STM)

The quantum-mechanical phenomenon of electron tunneling had been known for a long time, but the use of this phenomenon for the imaging of a conducting surface on atomic scale was only realized in 1982 when the first scanning tunneling microscope was built by Binnig et al.[112] At present, STM is a powerful tool for analyzing metallic and semiconducting surfaces.

A probe tip, usually made of W or Pt-Ir alloy, is attached to a piezodrive, which consists of three mutually perpendicular piezoelectric transducers. Using the coarse positioner and the *z* piezo, the tip and sample are brought to within a few angstroms of each other. The electron wavefunctions in the tip overlap electron wavefunctions in the sample surface. When a bias voltage is applied between the tip and the sample, an electric current will flow. The tunneling current is amplified by the current amplifier to become a voltage, which is compared with a reference value. The difference is then amplified again to drive the *z* piezo. The phase of the amplifiers is chosen to provide negative feedback. If the tunneling current is larger than the reference value, then the voltage applied to the *z* piezo tends to withdraw the tip from the sample surface, and vice versa. Therefore, an equilibrium *z* position is established through the feedback loop. As the tip scans over the sample surface, a two-dimensional array of equilibrium *z* positions, representing a contour plot of the equal tunneling-current surface, is obtained and stored. Ideally tips for STM should be monoatomically sharp apex. However, for most STM applications, tips prepared by mechanical cutting or by electrochemical etching are used.

It is clear that the tunneling current is extremely sensitive to a minute variance of the tip-sample distance. In order to achieve a stable metal-vacuum-metal tunneling, the suppression of environmental vibration is extremely important.[113, 114]

3.3 Experimental Section

3.3.1 Materials and Molecular Gold Rectangle

4,4'-bipyridine (bipy) was obtained from Aldrich and used as received. The molecular gold rectangle, $[Au_4(\mu\text{-PAnP})_2(\mu\text{-bipy})_2](OTf)_4$, was synthesized according to literature procedure.[32]

3.3.2 Substrate Pretreatment

Gold substrates

The gold substrates used for XPS characterization and ellipsometry measurements were gold-coated silicon wafers (Platypus Technologies). The substrates were cleaned immediately prior to use with "piranha" solution (3:1 concentrated H_2SO_4/30% H_2O_2) followed by thorough rinsing with ultrapure Milli-Q water.

Glass substrates

Microscope slides were cut into pieces of 1.5 x 0.9 cm and cleaned with dichloroethane, ethanol, acetone, and finally rinsed with ultrapure Milli-Q water.

Diamond substrates

Undoped nanocrystalline (u-NCD) diamond of 2.5 μm thickness was deposited on p-doped Si(001) substrates which have been pretreated in a diamond powder/ isopropanol slurry with an ultrasonic technique. The deposition was performed by a modified hot filament process with a CH_4 concentration of 2.91% in hydrogen. The substrate temperature as measured by a thermocouple (type K, Chromel/Alumel) was about 780 °C.

The 50 μm thick polycrystalline boron doped diamond (BDD) films were grown on *p*-type Si substrates in a commercial 2.45 GHz microwave plasma reactor (Astex) using methanol and boron oxide mixtures. The BDD samples had a surface resistance of 10 Ω cm, and the boron doping level was approximately 1020 cm^{-3}.

Acid cleaning and hydrogen plasma cleaning of diamond were performed for all diamond samples. Metallic impurities were first removed by aqua regia (3:1 concentrated HNO_3/concentrated HCl), followed by the removal of organic impurities from the diamond samples using "piranha" solution (3:1 concentrated H_2SO_4/30% H_2O_2). This will result in an oxidized diamond surface as evident in the increased hydrophilicity. H-termination of diamond samples was performed by microwave hydrogen plasma treatment using 800 W microwave power and 300 sccm of hydrogen gas flow for 15 min.

3.3.3 Instrumentation

X-ray photoelectron spectroscopy

XPS was performed with a Phobios 100 electron analyzer (SPECS GmbH), using an unmonochromated Mg Kα X-ray source (1253.6 eV). The pass energy of the hemisphere analyzer was set at 50 eV for wide scan and 20 eV for narrow scan, while the takeoff angle was fixed normal to the sample.

The samples for the XPS experiments were prepared by immersing cleaned u-NCD and gold substrates into a 10^{-6} M dichloromethane solution containing the gold rectangle for 10 min and rinsing thoroughly with ultrapure Milli-Q water. All solvents evaporated thoroughly before the XPS experiments.

XPS result does not depend on the method of sample preparation. Same results were obtained when a drop of dichloromethane solution containing the gold rectangle were deposited onto the substrate.

Ellipsometry

Ellipsometry measurements were performed at RT in the visible range using a spectroscopic ellipsometer, M-2000V from J. A. Woollam Co., Inc. The angle of incidence was set at 70º and the spectral range of 400 - 800 nm to measure the layer thickness. Ellipsometric modeling was performed using the WVASE software (J. A. Woollam Co., Inc.).

For thickness determination of the molecular thin film, a two-layer model was used (silicon substrate/gold/molecular film/ambient). Optical data for gold provided with the WVASE software was used and data for molecular film were fitted using Cauchy model.

The samples for ellipsometry measurements were prepared by immersing the gold substrate into a 10^{-6} M dichloromethane solution of the rectangle for 7-10 min. The samples will then be rinsed thoroughly with ultrapure Milli-Q water. All solvents evaporated thoroughly before the ellipsometry measurement.

Fluorescence Spectroscopy

Fluorescence spectra were recorded on a Perkin-Elmer LS55B spectrofluorophotometer equipped with a solid state sample holder.

The samples were prepared by depositing a drop of dichloromethane solution containing the gold rectangle (10μL, 10^{-4} M) onto cleaned u-NCD, BDD, gold and glass substrates. The fluorescence spectra were collected after the solvent has evaporated.

Scanning Tunneling Microscopy

The samples of $[Au_4(\mu\text{-PAnP})_2(\mu\text{-bipy})_2](OTf)_4$ for STM observation were prepared by directly depositing a drop of dichloromethane solution containing the gold rectangle (5μl; 10^{-6} M) on an atomically flat surface of freshly cleaved HOPG. After evaporation of the solvent, the STM images were recorded with PSIA XE-100 at ambient conditions. The tunneling tips were prepared by mechanically cutting Pt/Ir wire (90/10). The images were recorded in constant current mode.

3.4 Results and Discussion

3.4.1 X-ray Photoelectron Spectroscopy of $[Au_4(\mu\text{-PAnP})_2(\mu\text{-bipy})_2](OTf)_4$ (3)

XPS was performed to verify the elemental composition of **3**. The binding energy of the respective peak components gives information about the chemical state of emitting atom as well as its chemical environment. Hence, the chemical integrity of **3** can be evaluated.

In order to evaluate the overall quality of the sample, an overview spectrum was taken. Besides a large C 1s signal originating from the underlying diamond substrate, the spectrum contained three features that can be assigned to Au 4f, N 1s and P 2p signals of the gold rectangle. To derive precise information of the chemical nature of these elements, the individual element spectra were collected. Figure 3.4 shows the XPS spectrum in Au 4f core level region of **3**. The strong doublet peaks at 89.3 and 85.6 eV are attributed to one gold species.

The doublet is shifted by 2.5 eV to a higher binding energy as compare to the binding energy of gold element. Small shifts in binding energy are due to changes in oxidation state as well as the local chemical environment of the atom. When the atom's valence electron density is drawn away by another electronegative atom, the decreased valence electrons density around its atomic core is accompanied by a lower ability to screen core charge. This is known as 'loss of electronic screening'. This in turn leads to a higher binding energy of the core electrons. From the structure of **3**, Au is bound to N atom. Due to the high electronegativity of nitrogen and the expected large charge transfer from Au to N, Au should have a higher binding energy. Therefore, the higher binding energy of

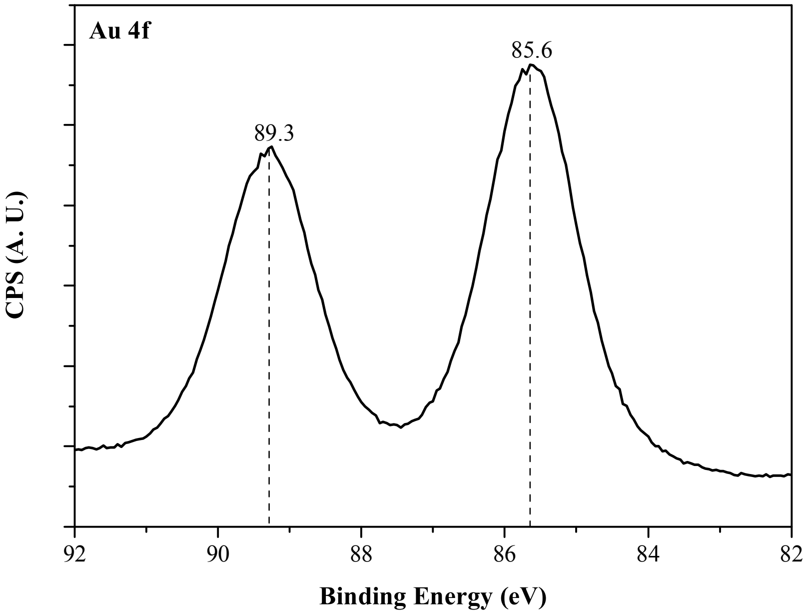

Figure 3.4 XPS spectra of the gold rectangle on u-NCD in Au 4f core level region collected at normal emission.

the Au 4f spectrum suggests that the gold rectangle is intact when adsorbed onto the diamond substrate. To further confirm that the rectangle remains intact, an XPS spectrum of a decomposed gold rectangle was taken. The spectrum in Figure 3.5 shows two asymmetrical peaks. The peaks can be resolved into two sets of doublet. The larger doublet pair (red) has a lower binding energy at 87.6 and 84 eV and is attributed to the decomposed rectangle. This proves that the decomposed rectangle has a different binding energy as that of the intact rectangle. The other set of doublet (blue) is attributed to some remaining gold rectangles which have not decomposed. The other two features seen are the N 1s and P 2p signals which are shown in Figures 3.6. and 3.7 respectively.

The gold rectangle was also adsorbed onto gold substrate. The Au 4f core level region is shown in Figure 3.8. The spectrum reveals two doublets. The main signal at 89.7 and 86.1 eV is attributed to the gold rectangle. The other signal originates from the gold substrate. The binding energy of the main signal also suggests that the gold rectangle is intact upon adsorption onto the gold substrate.

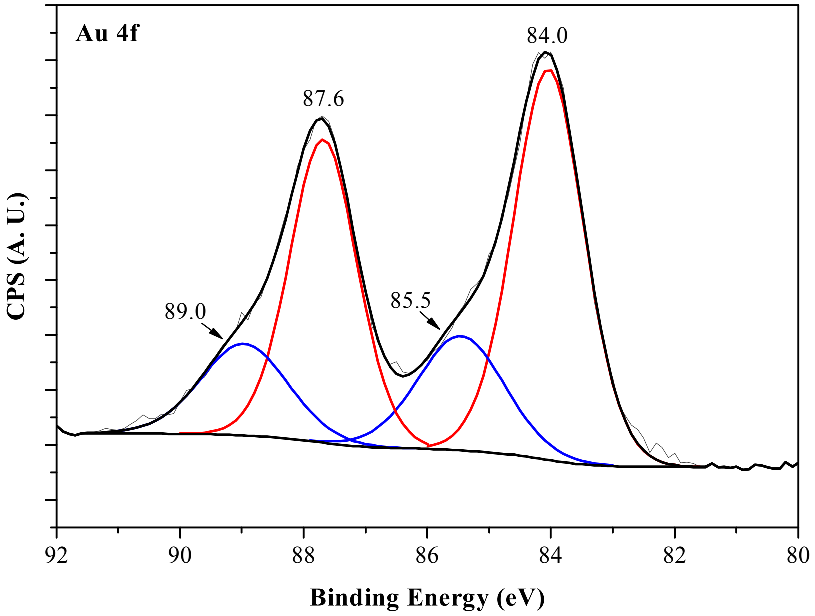

Figure 3.5 XPS spectra of a decomposed gold rectangle in Au 4f core level region collected at normal emission. The low energy component (red) stems from the gold of the decomposed gold rectangle. The other set of doublet (blue) is due to remaining gold rectangles that have not been decomposed.

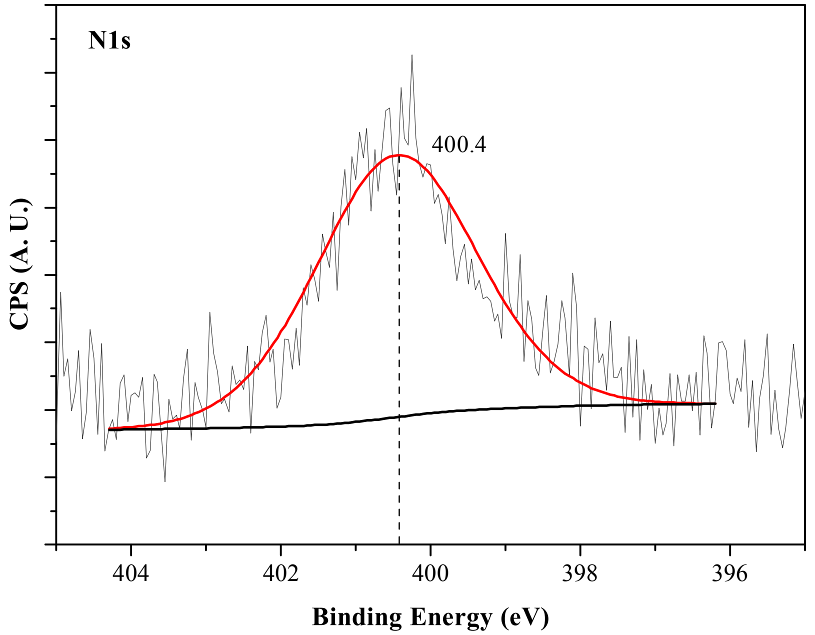

Figure 3.6 XPS spectra in N 1s core level region collected at normal emission.

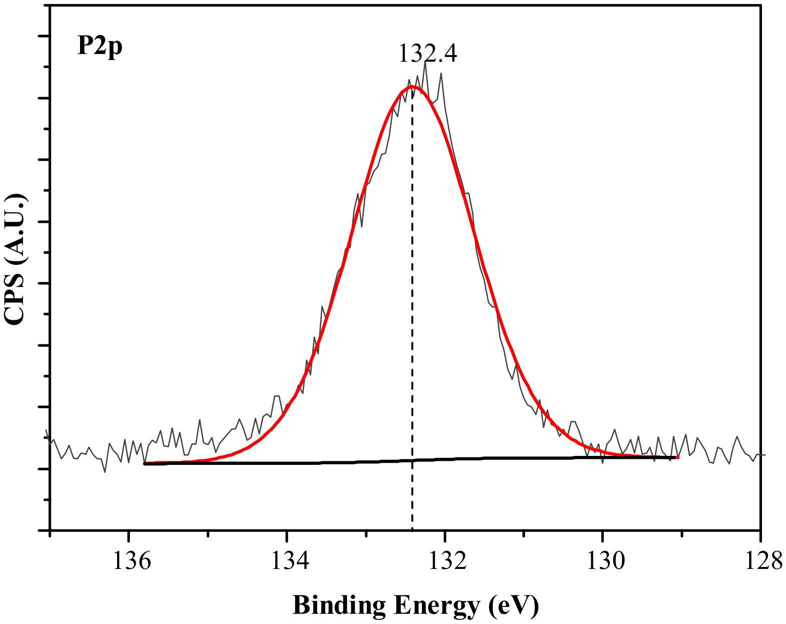

Figure 3.7 XPS spectra in P 2p core level region collected at normal emission.

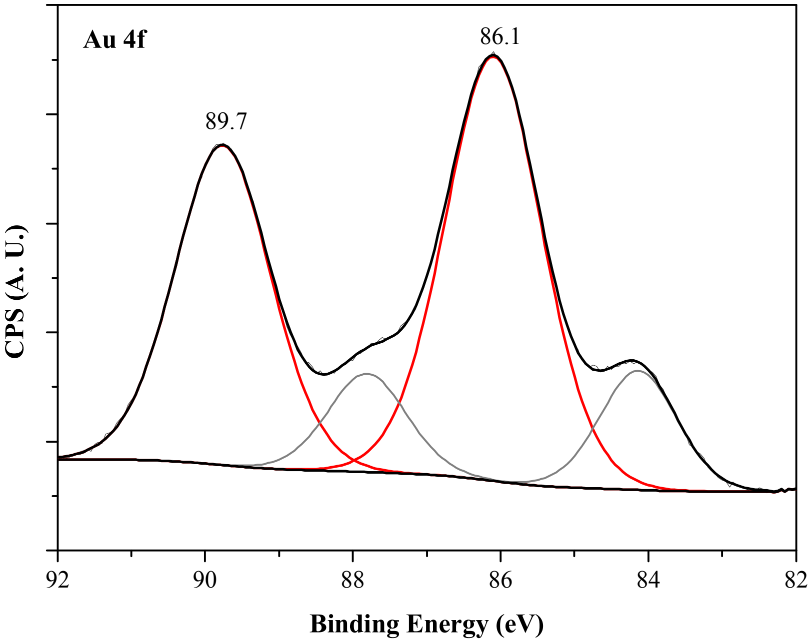

Figure 3.8 XPS spectra of the gold rectangle on gold substrate. The Au 4f core level region collected at normal emission is shown here. The lower energy doublet (grey) is attributed to the gold substrate. The strong intense doublet stems from the gold rectangle.

3.4.2 Fluorescence Spectroscopy

In solution, the gold rectangle gives an emission peak at 480 nm when irradiated at 420 nm. The fluorescence spectra of the gold rectangles when absorbed onto different substrates are shown in Figure 3.9.

Glass is an insulator and it is known that it does not quench any emission. As expected, there is a peak at 480 nm. However, when the gold rectangle is absorbed onto u-NCD, BDD and gold substrates, the fluorescence is quenched. This indicates that there is electron or energy transfer between the molecule and substrate. Gold and u-NCD are conducting substrates, while BDD is considered to be a semi-conductor. It is possible that the fluorescence of the gold rectangle will be quenched on all conducting and semi-conducting substrates.

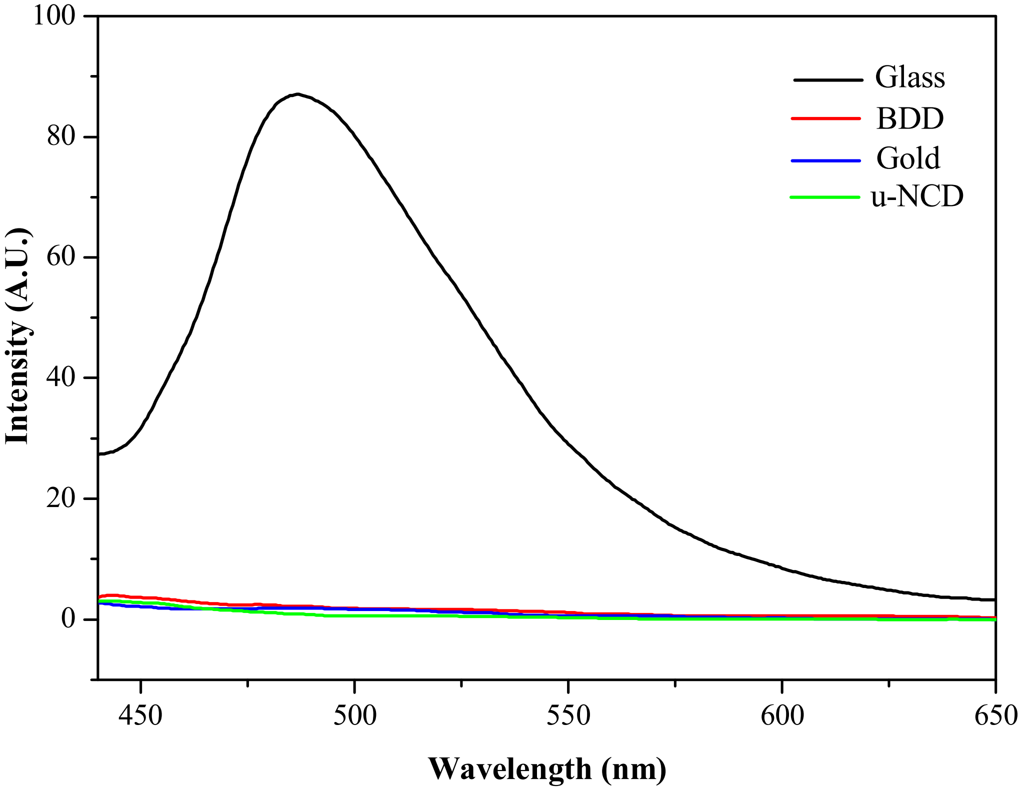

Figure 3.9 Emission spectra of **3** on various substrates.

3.4.3 Ellipsometry

The interaction between the gold rectangle and substrate is weak van der Waals forces. The gold rectangle is adsorbed onto the substrate through physisoption. It is possible for the gold rectangle to form surface clusters or multilayer on the substrate. The formation of monolayer depends on the solution concentration and the time in which the substrate was immersed in the solution. Ellipsometry is sensitive to thin-film characteristic such as film thickness. Therefore, it was used to estimate the conditions needed to produce a monolayer.

The concentration of the solution was set at 10^{-6} M. At lower concentration, the gold rectangle tends to dissociate. The time of immersion was varied and the film thicknesses as estimated by the fitting are shown in **Table 3.1**.

Based on the dimension of the gold rectangle (Figure 3.10) and the film thickness at 8 min immersion time, the result suggests that the gold rectangle is lying flat on the gold substrate forming a monolayer. At immersion time > 8 min, multi molecular adlayers were formed. Accurate fitting could not be done for immersion time at 7 min or lower. This could be due to only small domains of the gold substrate were covered with the rectangle and thus the imperfections of the layer greatly affect the measurement and fitting.

Table 3.1 Fitted film thickness at different immersion time

Time of immersion (min)	Film thickness (nm)
10	1.370 ± 0.00919
9	1.289 ± 0.00622
8	0.715 ± 0.00616
7	a

[a] Accutre fitting could not be done

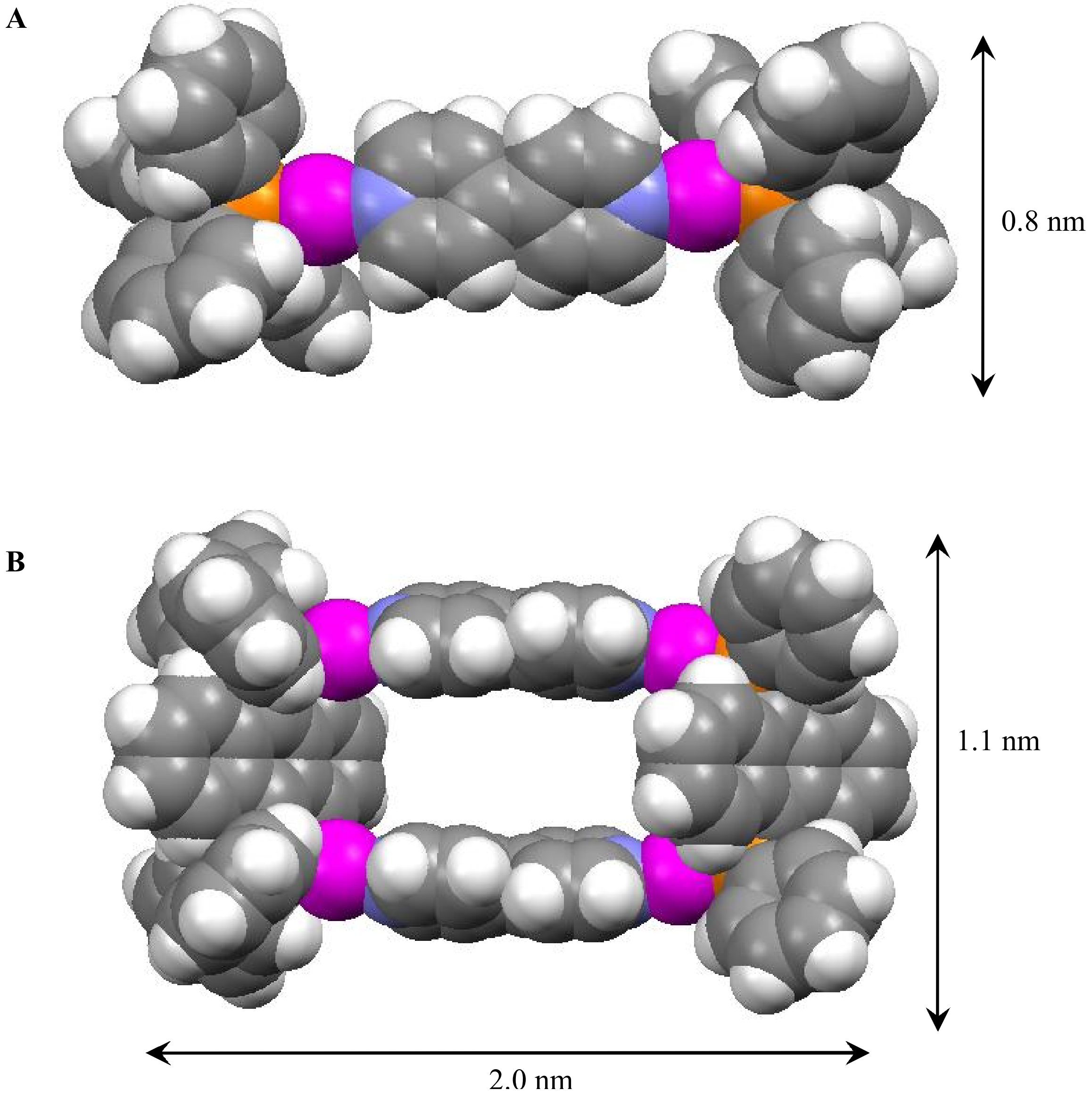

Figure 3.10 Space-filling model of **3** from a side (A) and top (B) view of the rectangle.

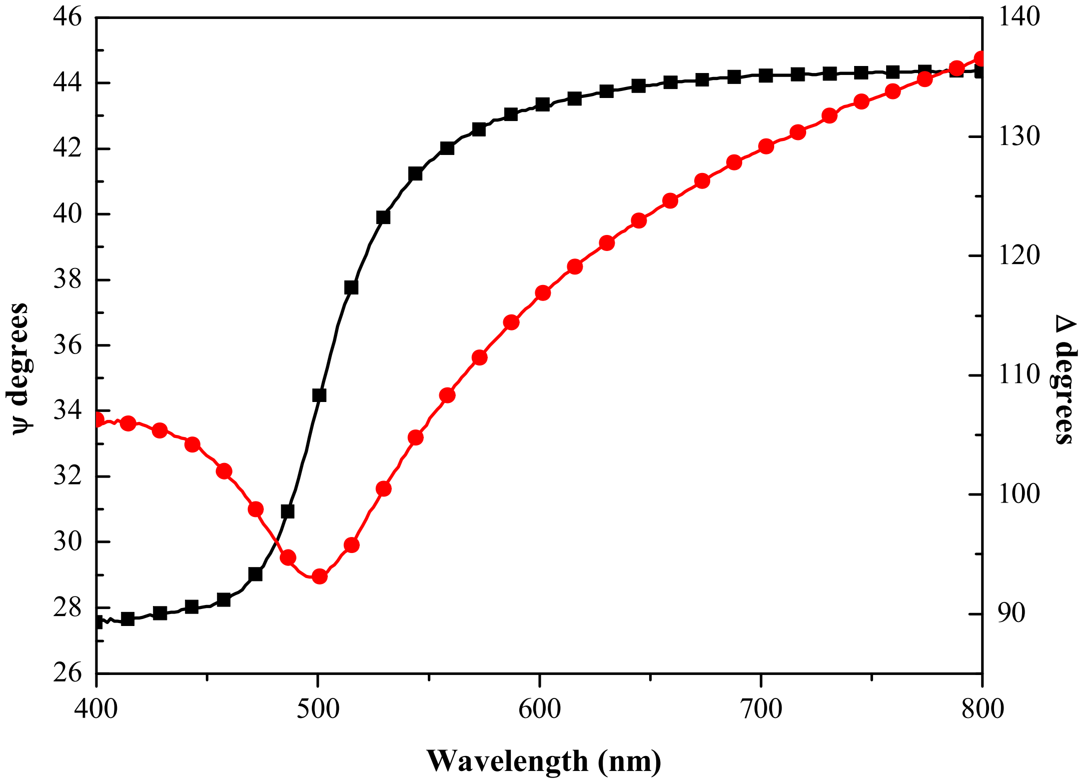

Figure 3.11 Measured Ψ (—●—) and Δ (—■—) data at 10 min immersion time. Solid lines show best-fit calculations to the Cauchy-model.

The solid lines in Figure 3.11 show results of the Cauchy-model best-fit calculations for a thin film of **3** at 10 min immersion time. The measured Ψ and Δ data are plotted as symbols. The fittings for the experimental data for immersion time 8 – 10 min are good and with mean square error (MSE) < 10.

3.4.3 Scanning Tunneling Microscopy

STM has proven to be a powerful tool for characterizing supramolecular self-assemblies on surfaces, formed via self-organization.[77] A substrate which is commonly used is highly oriented pyrolytic graphite (HOPG). HOPG possesses a few unique properties such as being a chemical inert conductor and an easy to prepare clean surface with flat terrace over several 100 nm.

A high resolution STM image of a freshly cleaved HOPG surface was recorded and shown in Figure 3.12. The STM image does not show very clearly each graphite atoms as it was recorded in open atmosphere. However, the line profile of the indicated line shows atomic resolution of the HOPG surface.

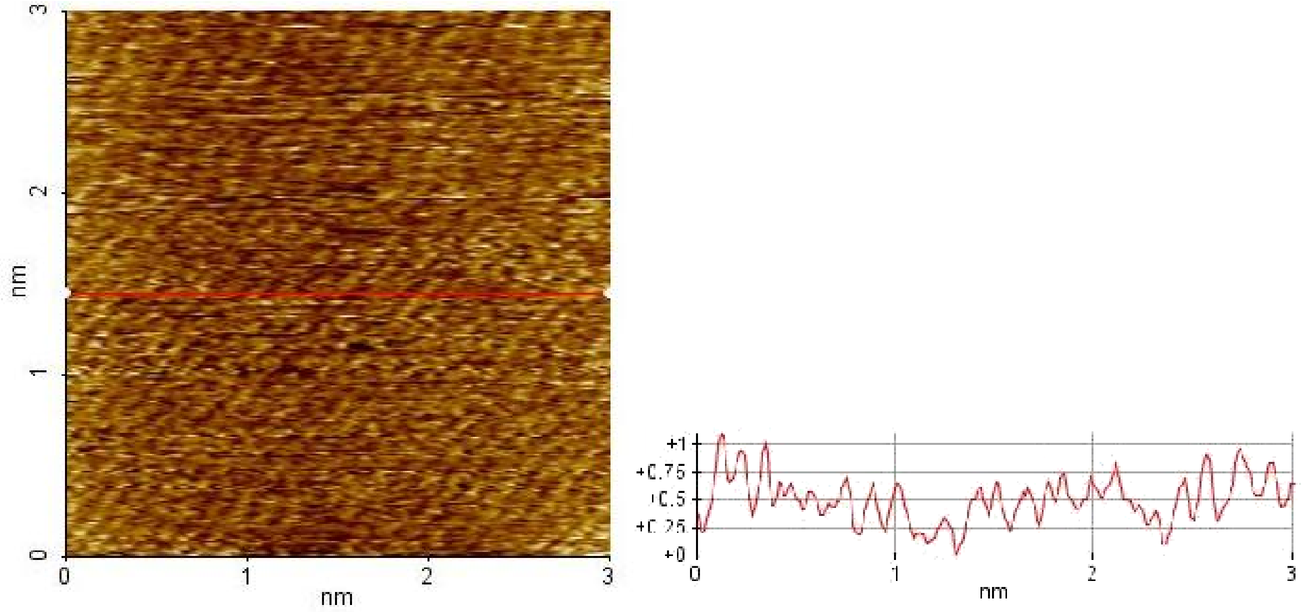

Figure 3.12 Left: High resolution STM image of bare HOPG (3.0 nm x 3.0 nm, V_{bias} = 0.1 V, I_{set} = 2.0 pA). Right: Line profile along the indicated line.

Solution concentration is critical in forming a monolayer on HOPG surface. At concentration > 10^{-5} M, surface clusters were formed because of the charge character of the molecules. A low resolution STM image of the molecular adlayer on HOPG is shown in Figure 3.13. The molecular network extends as a single domain over an area of 50 x 50 nm^2. The molecular adlayer consists of wide bands. From the line profile of the image, each band is 2.0 nm wide. This is consistence with the length of the gold rectangle. The dimensions of the gold rectangle were independently determined through x-ray crystallography and are shown in Figure 3.10. However, clear high resolution STM images were not obtained. It is not clear from the image if the gold rectangles were lying flat on the substrate or on its side.

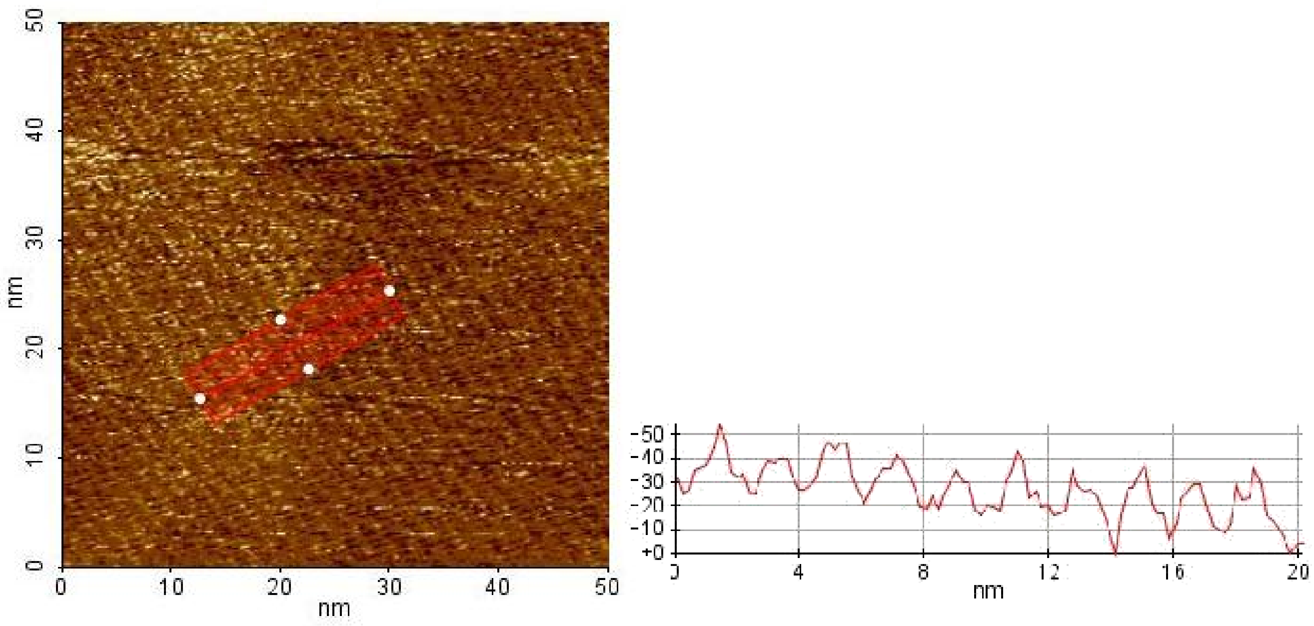

Figure 3.13 Left: Low resolution STM image of ordered assembly of **3** (50 nm x 50 nm, V_{bias} = 0.25 V, I_{set} = 0.1 nA). Right: Average Line profile along the indicated line.

3.5 Conclusion

In this chapter, we have presented the self-organization of a Au^I molecular rectangle, $[Au_4(\mu\text{-PAnP})_2(\mu\text{-bipy})_2](OTf)_4$, on several substrates. The formation of monolayer was done through immersion and drop casting methods. The film thickness was estimated through ellipsometry. The results show a simple method of controlling the layer uptake by varying the time of immersion. XPS analysis was done to confirm the chemical integrity of the adsorbed molecules. The results reveal that the gold rectangle remains intact upon adsorption. The interaction between molecule and substrate was investigated through surface fluorescence. The fluorescence of the gold rectangle was quenched when adsorbed onto conducting and semi-conducting substrates. This suggests that there are electron or energy transfer between the molecule and substrate. Lastly, scanning tunneling microscopy reveals a well ordered 2D adlayer of gold rectangle on HOPG.

CONCLUSION

In conclusion, we have shown the synthesis of two Au^I molecular rectangles, $[Au_4(\mu\text{-PAnP})_2(\mu\text{-DPE})_2](OTf)_4$ and $[Au_4(\mu\text{-PAnP})_2(\mu\text{-BPE})_2](OTf)_4$. Both rectangles are emissive and display a fluorescence peak at 480 nm. Their fluorescence is quenched upon binding with aromatic guests. Fluorescence titration was used to determine the binding constants with guests. The binding constants were low as the molecular rectangles have large cavities. However, the prospect of binding larger guest molecules is possible with the large cavity.

Secondly, we have shown the self-organization of a molecular rectangle, $[Au_4(\mu\text{-PAnP})_2(\mu\text{-bipy})_2](OTf)_4$, on surfaces. XPS measurements allowed the study of the stability of the gold rectangle when it was adsorbed onto the substrates. The gold rectangles did not dissociate. The thickness of the molecular thin film was measured by ellipsometry. The results suggest that the molecular rectangle lies flat on the gold substrate. STM images also revealed a well assembled monolayer of the gold rectangle on HOPG.

With the knowledge of how to form a well ordered monolayer of the gold rectangle, it is logical to study the system further. The effects of the substrates on the binding of the gold rectangle with guests have yet to be studied and it may provide valuable insights to application such as devising of molecular sensors.

APPENDICES

Table A1 X-ray crystal data of **1** and **2**

Compounds	**1**	**2**
empirical formula	$C_{55}H_{38}Au_2Cl_6F_6N_2O_6P_2S_2$	$C_{107}H_{56}Au_4Cl_8F_9N_4O_{12.50}P_4S_4$
formula weight	1669.57	3092.14
T (K)	295(2)	296(2)
cryst. syst.	Triclinic	Orthorhombic
Space group	P-1	Pbam
a (Å)	12.855(9)	18.8682(16)
b (Å)	18.589(13)	27.517(3)
c (Å)	19.771(13)	29.199(2)
α (deg)	115.709(12)	90
β (deg)	99.824(13)	90
γ (deg)	92.573(14)	90
V (Å^3)	4156(5)	15160(2)
Z	2	4
calcd. ρ (Mg/m^3)	1.334	1.355
μ (mm-1)	3.857	4.153
F(000)	1612	5932
reflections collected	44103	67991
independent reflections	14634	13482
goodness-of-fit	0.922	0.974
R1[a]	0.0906	0.0874
wR2[a]	0.2424	0.2701

[a] $R1 = (||Fo| - |Fc||)/(|Fo|)$; $wR2 = [w(Fo^2 - Fc^2)/w(Fo4)]^{1/2}$

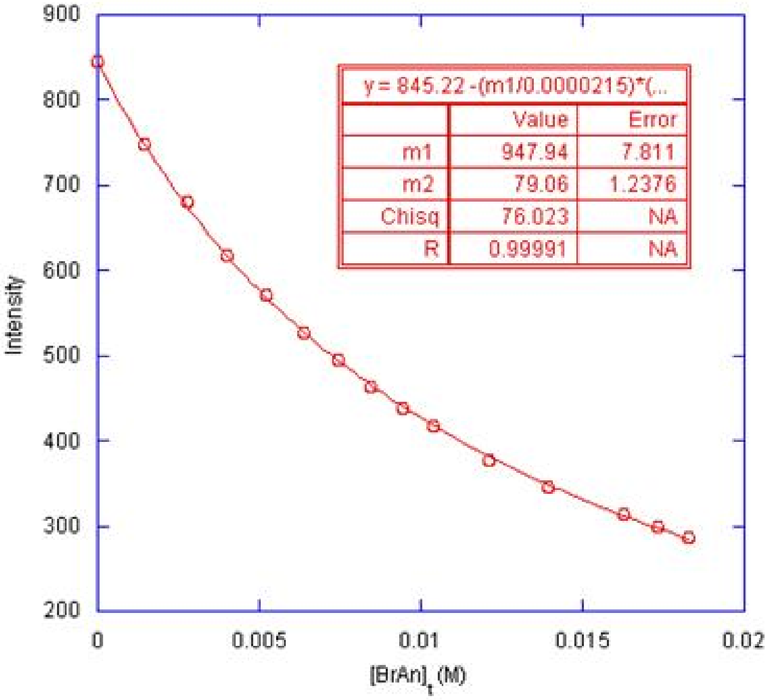

y = 845.22 -(m1/0.0000215)*(...

	Value	Error
m1	947.94	7.811
m2	79.06	1.2376
Chisq	76.023	NA
R	0.99991	NA

Figure A1 Emission titration curve upon addition of BrAn to a CH_3CN solution of **1.** Line shown is the least square fit using equation 1.

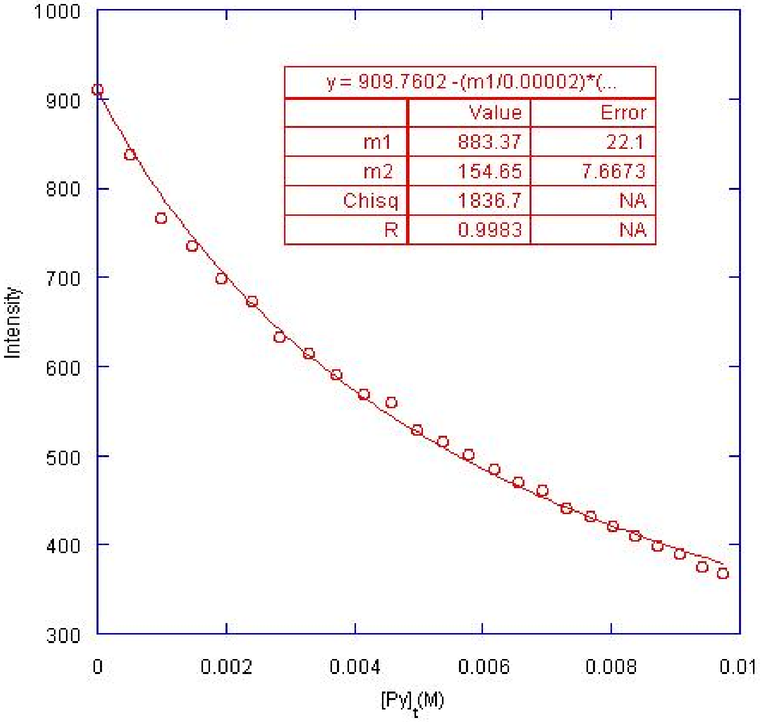

y = 909.7602 -(m1/0.00002)*(...

	Value	Error
m1	883.37	22.1
m2	154.65	7.6673
Chisq	1836.7	NA
R	0.9983	NA

Figure A2 Emission titration curve upon addition of Py to a CH_3CN solution of **1.** Line shown is the least square fit using equation 1.

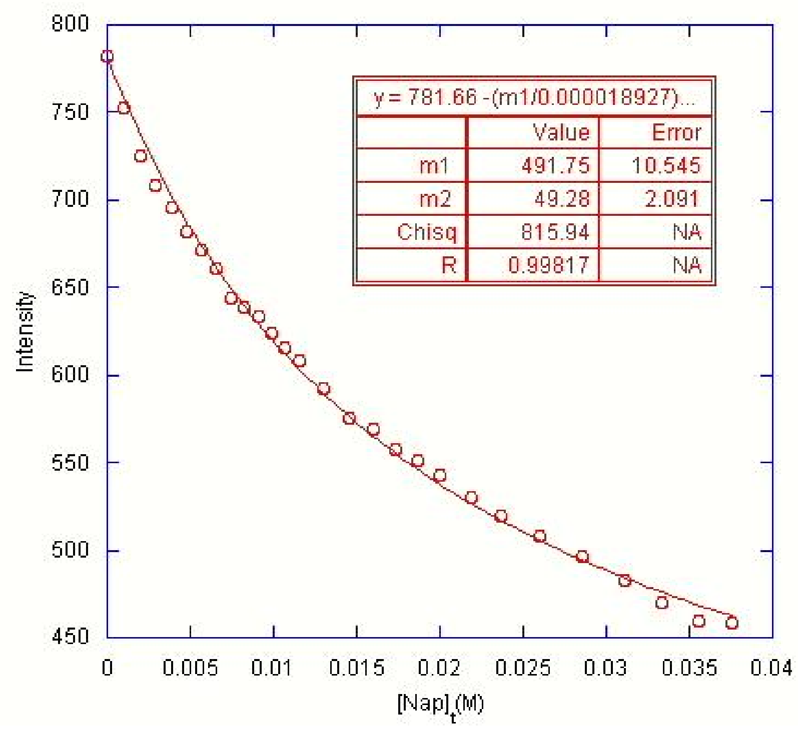

y = 781.66 -(m1/0.000018927)...	Value	Error
m1	491.75	10.545
m2	49.28	2.091
Chisq	815.94	NA
R	0.99817	NA

Figure A3 Emission titration curve upon addition of Nap to a CH_3CN solution of **1.** Line shown is the least square fit using equation 1.

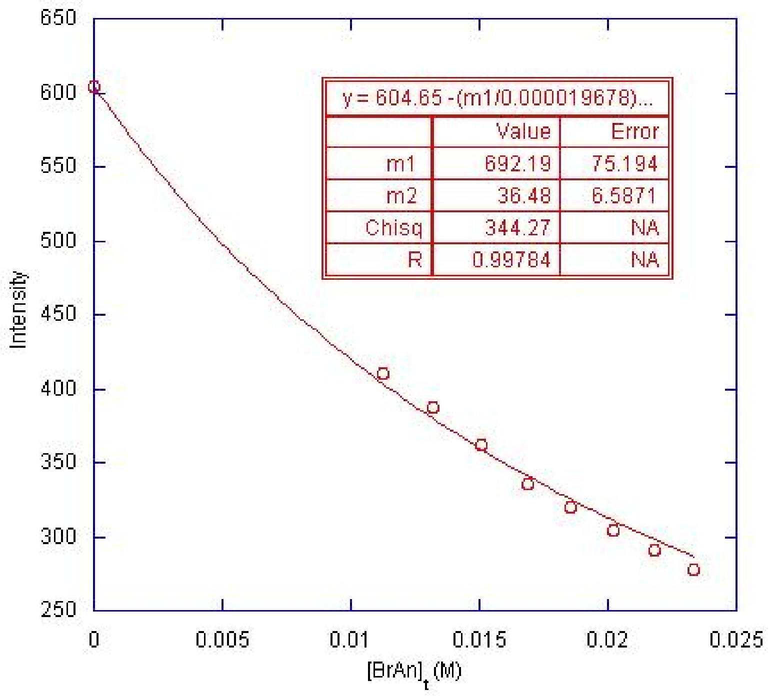

y = 604.65 -(m1/0.000019678)...	Value	Error
m1	692.19	75.194
m2	36.48	6.5871
Chisq	344.27	NA
R	0.99784	NA

Figure A4 Emission titration curve upon addition of BrAn to a CH_3CN solution of **2.** Line shown is the least square fit using equation 1.

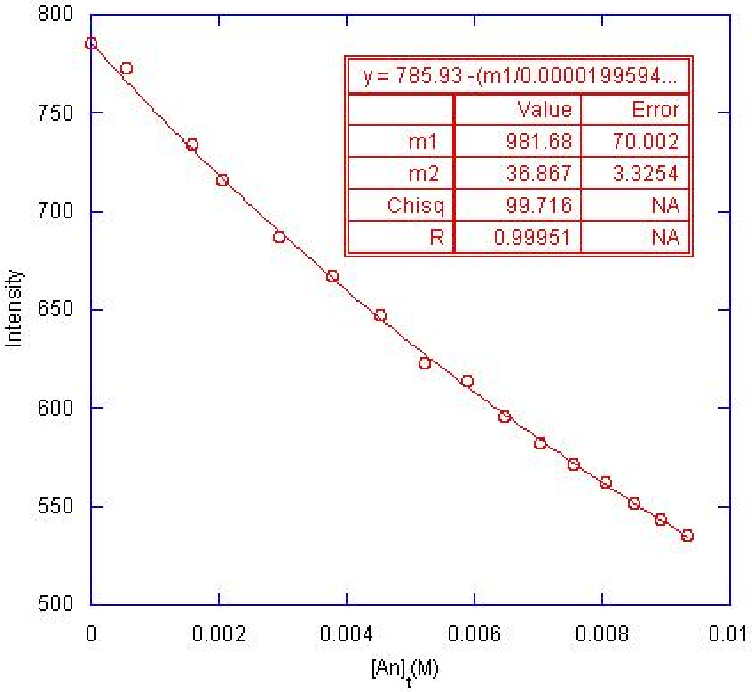

Figure A5 Emission titration curve upon addition of An to a CH_3CN solution of **2.** Line shown is the least square fit using equation 1.

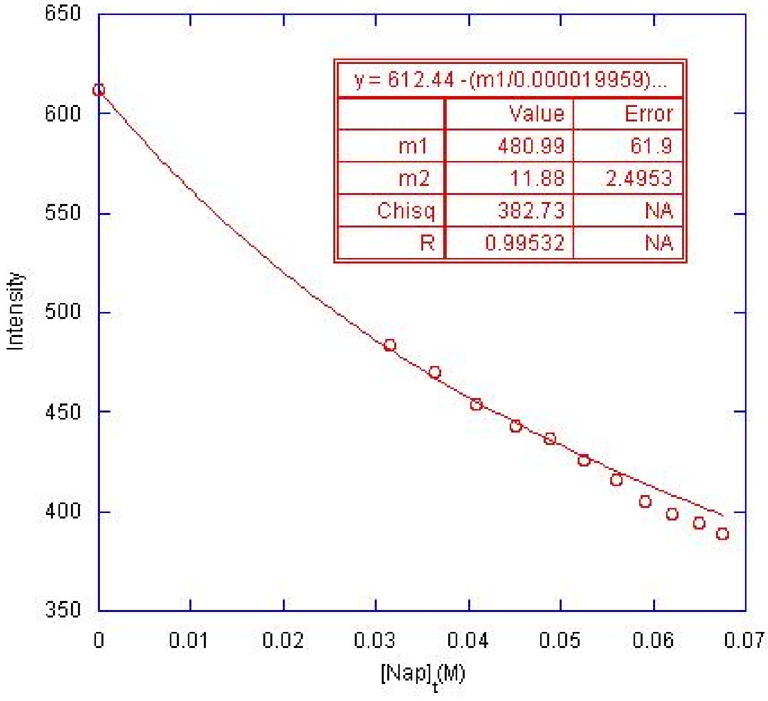

Figure A6 Emission titration curve upon addition of Nap to a CH_3CN solution of **2.** Line shown is the least square fit using equation 1.

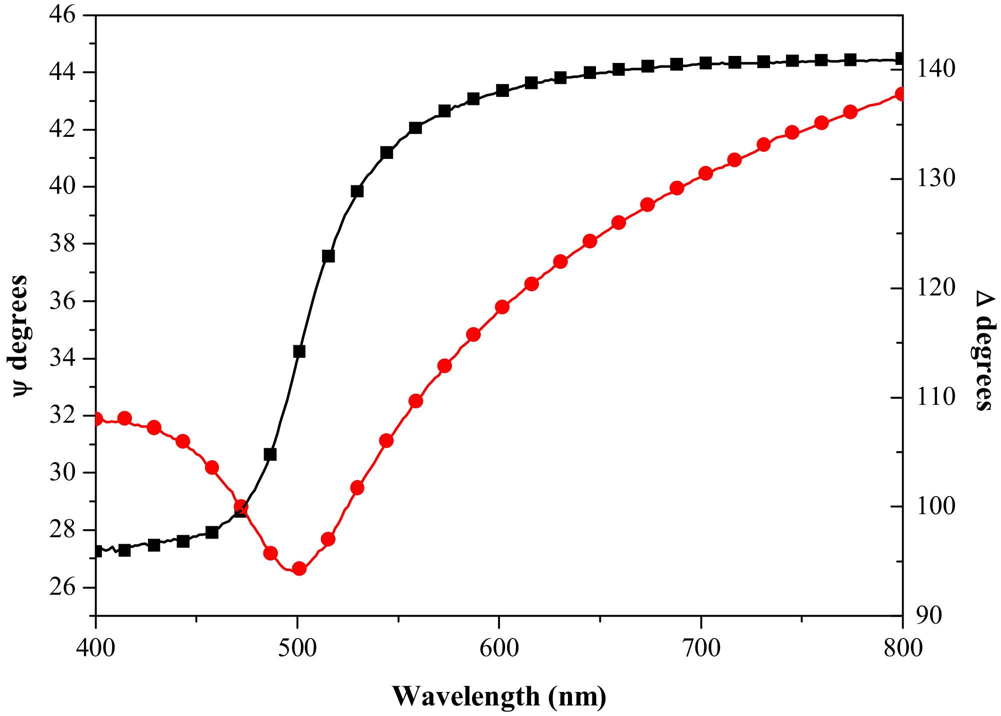

Figure A7 Measured Ψ (●) and Δ (■) data at 9 min immersion time. Solid lines show best-fit calculations to the Cauchy-model.

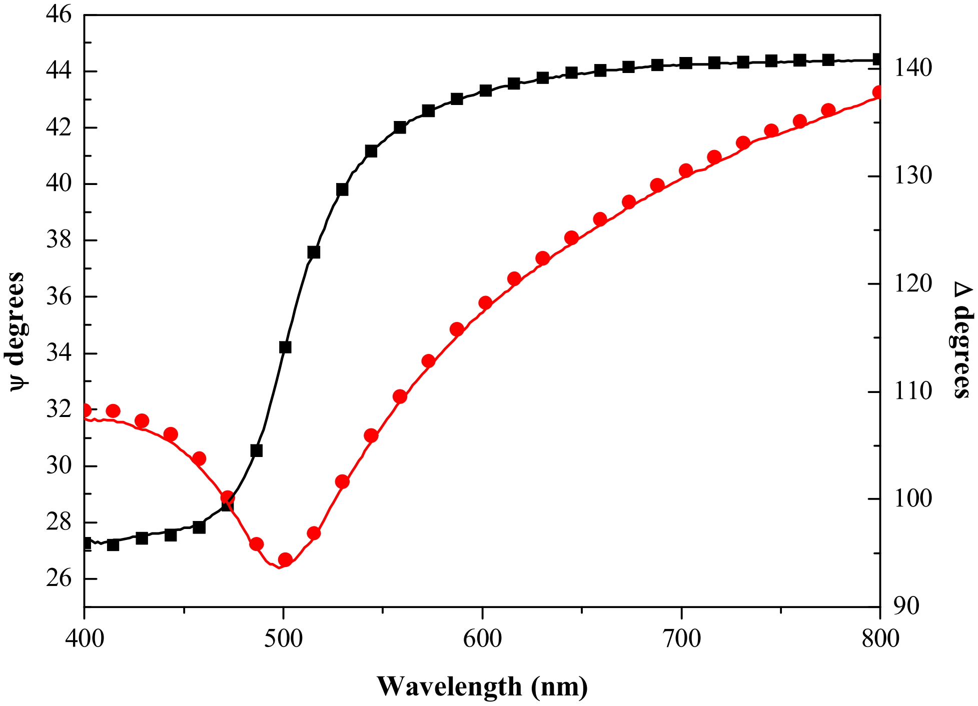

Figure A8 Measured Ψ (●) and Δ (■) data at 8 min immersion time. Solid lines show best-fit calculations to the Cauchy-model.

REFERENCES

1. Lehn, J.-M., *Chem. Soc. Rev.* **2007,** *36* (2), 151-160.
2. Seidel, S. R. S., Peter J., *Acc. Chem. Res.* **2002,** *35* (11), 972-983.
3. Holliday, B. J.; Mirkin, C. A., *Angew. Chem., Int. Ed.* **2002,** *40* (11), 2022-2043.
4. Caulder, D. L.; Raymond, K. N., *J. Chem. Soc., Dalton Trans.* **1999,** (8), 1185-1200
5. Baker, A. T.; Crass, J. K.; Maniska, M.; Craig, D. C., *Inorg. Chim. Acta* **1995,** *230* (1-2), 225-229.
6. Fujita, M., *J. Synth. Org. Chem. Jpn.* **1996,** *54* (11), 953-963.
7. Fujita, M.; Sasaki, O.; Mitsuhashi, T.; Fujita, T.; Yazaki, J.; Yamaguchi, K.; Ohura, K. *J.*, *Chem. Soc., Chem. Commun.* **1996,** (13), 1535-1536
8. Lai, S.-W.; Chan, M. C.-W.; Peng, S.-M.; Chi-Ming Che, *Angew. Chem., Int. Ed.* **1999,** *38* (5), 669-671.
9. Lee, S. B.; Hwang, S.; Chung, D. S.; Yun, H.; Hong, J.-I., *Tetrahedron Lett.* **1998,** *39* (8), 873-876.
10. Schnebeck, R.-D.; Randaccio, L.; Zangrando, E.; Lippert, B., *Angew. Chem., Int. Ed.* **1998,** *37* (1-2), 119-121.
11. Schweiger, M.; Seidel, S. R.; Arif, A. M.; Stang, P. J., *J. Inorg. Chem.* **2002,** *41* (9), 2556-2559
12. Sun, S.-S.; Lees, A. J., *J. Am. Chem. Soc.* **2000** *122* (37), 8956-8967.
13. Sun, S.-S.; Lees, A. J., *Organometallics* **2002,** *21* (1), 39-49.
14. Fujita, M.; Yazaki, J.; Ogura, K., *J. Am. Chem. Soc.* **1990,** *112* (14), 5645-5647.
15. Stang, P. J.; Chen, K.; Arif, A. M., *J. Am. Chem. Soc.* **1995,** *117* (34), 8793-8797.

16. Fujita, M.; Ibukuro, F.; Yamaguchi, K.; Ogura, K., *J. Am. Chem. Soc.* **1995,** *117* (14), 4175-4176.

17. Jeong, K.-S.; Cho, Y. L.; Chang, S.-Y.; Park, T.-Y.; Song, J. U., *J. Org. Chem.* **1999,** *64* (26), 9459-9466

18. Hasenknopf, B.; Lehn, J.-M.; Kneisel, B. O.; Baum, G.; Dieter Fenske, *Angew. Chem., Int. Ed. Engl.* **1996,** *35* (16), 1838-1840.

19. Mamula, O.; Zelewsky, A. v.; Gérald Bernardinelli, *Angew. Chem., Int. Ed.* **1998,** *37* (3), 289-293.

20. Stang, P. J.; Persky, N. E.; Manna, J., *J. Am. Chem. Soc.* **1997,** *119* (20), 4777-4778.

21. Fujita, M.; Ibukuro, F.; Hagihara, H.; Ogura, K., *Nature* **1994,** *367* (6465), 720-723.

22. Yip, J. H. K.; Prabhavathy, J., *Angew. Chem., Int. Ed.* **2001,** *40* (11), 2159-2162.

23. Beissel, T.; Powers, R. E.; Raymond, K. N., *Angew. Chem., Int. Ed. Engl.* **1996,** *35* (10), 1084-1086.

24. Fujita, M.; Oguro, D.; Miyazawa, M.; Oka, H.; Yamaguchi, K.; Ogura, K., *Nature* **1995,** *378* (6556), 469-471.

25. Jacopozzi, P.; Dalcanale, E., *Angew. Chem., Int. Ed. Engl.* **1997,** *36* (6), 613-615.

26. Olenyuk, B.; Whiteford, J. A.; Fechtenkotter, A.; Stang, P. J., *Nature* **1999,** *398* (6730), 796-799.

27. Balch, A. L.; Olmstead, M. M.; Vickery, J. C., *Inorg. Chem.* **1999,** *38* (15), 3494-3499.

28. Hunks, W. J.; MacDonald, M.-A.; Jennings, M. C.; Puddephatt, R. J., *Organometallics* **2000,** ***19*** (24), 5063 -5070.

29. Schmidbaur, H., *Gold: Progress in Chemistry, Biochemistry and Technology*. Wiley: Chichester: 1999.

30. Chan, W.-H.; Mak, T. C. W.; Che, C.-M., *J. Chem. Soc., Dalton Trans.* **1998**, 2275 - 2276

31. Shieh, S.-J.; Li, D.; Peng, S.-M.; Che, C.-M., *J. Chem. Soc., Dalton Trans.* **1993**, 195 - 196.

32. Lin, R.; Yip, J. H. K.; Zhang, K.; Koh, L. L.; Wong, K.-Y.; Ho, K. P., *J. Am. Chem. Soc.* **2004,** *126.*

33. Aoyagi, M.; Biradha, K.; Fujita, M., *J. Am. Chem. Soc.* **1999,** *121* (32), 7457-7458.

34. Biradha, K.; Seward, C.; Zaworotko, M. J., *Angew. Chem., Int. Ed.* **1999,** *38* (4), 492-495.

35. Yoshizawa, M.; Miyagi, S.; Kawano, M.; Ishiguro, K.; Fujita, M., *J. Am. Chem. Soc.* **2004,** *126* (30), 9172-9173

36. Yoshizawa, M.; Takeyama, Y.; Kusukawa, T.; Fujita, M., *Angew. Chem., Int. Ed.* **2002,** *41* (8), 1347-1349.

37. Ikeda, A.; Udzu, H.; Zhong, Z.; Shinkai, S.; Sakamoto, S.; Yamaguchi, K., *J. Am. Chem. Soc.* **2001,** *123* (17), 3872-3877.

38. Kuehl, C. J.; Kryschenko, Y. K.; Radhakrishnan, U.; Seidel, S. R.; Huang, S. D.; Stang, P. J., *Proc. Natl. Acad. Sci. U.S.A.* **2002** *99* (8), 4932-4936.

39. Kusukawa, T.; Fujita, M., *Angew. Chem., Int. Ed.* **1998,** *37* (22), 3142-3144.

40. Cram, D. J., *Angew. Chem., Int. Ed. Engl.* **1988,** *27* (8), 1009-1020.

41. Pedersen, C. J., *Angew. Chem., Int. Ed. Engl.* **1988,** *27* (8), 1021-1027.

42. Lehn, J.-M., *Angew. Chem., Int. Ed. Engl.* **1988,** *27* (1), 89-112.

43. Diederich, F., *Cyclophanes*. Royal Society of Chemistry: Cambridge: 1991.

44. Maverick, A. W.; Klavetter, F. E., *Inorg. Chem.* **1984** *23* (25), 4129-4130

45. Fujita, M.; Yazaki, J.; Ogura, K., *Tetrahedron Lett.* **1991,** *32* (40), 5589-5592.

46. Fujita, M.; Nagao, S.; Iida, M.; Ogata, K.; Ogura, K., *J. Am. Chem. Soc.* **1993,** *115* (4), 1574-1576.

47. Houghton, M. A.; Bilyk, A.; Harding, M. M.; Turner, P.; Hambley, T. W., *J. Chem. Soc., Dalton Trans.* **1997**, 2725 - 2734.

48. Xu, D.; Hong, B., *Angew. Chem., Int. Ed.* **2000,** *39* (10), 1826-1829.

49. Whiteford, J. A.; Lu, C. V.; Stang, P. J., *J. Am. Chem. Soc.* **1997,** *119* (10), 2524-2533

50. Holliday, B. J.; Farrell, J. R.; Mirkin, C. A.; Lam, K.-C.; Rheingold, A. L., *J. Am. Chem. Soc.* **1999,** *121* (26), 6316-6317.

51. Benkstein, K. D.; Hupp, J. T.; Stern, C. L., *Inorg. Chem.* **1998,** *37* (21), 5404-5405.

52. Chang, S.-Y.; Jeong, K.-S., *J. Org. Chem.* **2003,** *68* (10), 4014-4019.

53. Jeong, K.-S.; Cho, Y. L.; Song, J. U.; Chang, H.-Y.; Choi, M.-G., *J. Am. Chem. Soc.* **1998,** *120* (42), 10982-10983

54. Jeong, K.-S.; Choi, J. S.; Chang, S.-Y.; Chang, H.-Y**.**, *Angew. Chem., Int. Ed.* **2000,** *39* (9), 1692-1695

55. Whiteford, J. A.; Stang, P. J.; Huang, S. D., *Inorg. Chem.* **1998,** *37* (21), 5595-5601

56. Sommer, R. D.; Rheingold, A. L.; Goshe, A. J.; Bosnich, B., *J. Am. Chem. Soc.* **2001,** *123* (17), 3940-3952.

57. Cram, D. J., *Angew. Chem., Int. Ed. Engl.* **1986,** *25* (12), 1039-1057.

58. Benkstein, K. D.; Hupp, J. T.; Charlotte L. Stern, *Angew. Chem., Int. Ed.* **2000,** *39* (16), 2891-2893.

59. Kuehl, C. J.; Huang, S. D.; Stang, P. J., *J. Am. Chem. Soc.* **2001,** *123* (39), 9634-9641.

60. Kuehl, C. J.; Mayne, C. L.; Arif, A. M.; Stang, P. J., *Org. Lett.* **2000,** *2* (23), 3727-3729.

61. Lehn, J.-M., *Proc. Natl. Acad. Sci. U.S.A.* **2002,** *99* (8), 4763-4768.

62. Whitesides, G. M.; Boncheva, M., *Proc. Natl. Acad. Sci. U.S.A.* **2002,** *99* (8), 4769-4774.

63. Barth, J. V.; Weckesser, J.; Cai, C.; Günter, P.; Bürgi, L.; Jeandupeux, O.; Kern, K., *Angew. Chem., Int. Ed. Engl.* **2000,** *39* (7), 1230-1234.

64. Hipps, K. W.; Scudiero, L.; Barclow, D. E.; Cooke, M. P., Jr. , *J. Am. Chem. Soc.* **2002,** *124* (10), 2126-2127.

65. Scudiero, L.; Barlow, D. E.; Mazur, U.; Hipps, K. W., *J. Am. Chem. Soc.* **2001,** *123* (17), 4073-4080.

66. Yoshimoto, S.; Suto, K., Tada, A.; Kobayashi, N.; Itaya, K., *J. Am. Chem. Soc.* **2004,** *126* (25), 8020-8027.

67. Dinolfo, P. H.; Hupp, J. T., *Chem. Mater.* **2001,** *13* (10), 3113-3125.

68. Keefe, M. H.; Benkstein, K. D.; Hupp, J. T., *Coord. Chem. Rev.* **2000,** *205* (1), 201-228.

69. Slone, R. V.; Benkstein, K. D.; Bélanger, S.; Hupp, J. T.; Guzei, I. A.; Rheingold, A. L., *Coord. Chem. Rev.* **1998,** *171*, 221-243.

70. B. A. Hermann, L. J. S., C. E. Housecroft, E. C. Constable,, *Adv. Funct. Mater.* **2006,** *16* (2), 221-235.

71. Nuzzo, R. G.; Allara, D. L., *J. Am. Chem. Soc.* **1983,** *105* (13), 4481-4483.

72. Fernandez-Lopez, S.; Kim, H.-S.; Choi, E. C.; Delgado, M.; Granja, J. R.; Khasanov, A.; Kraehenbuehl, K.; Long, G.; Weinberger, D. A.; Wilcoxen, K. M.; Ghadiri, M. R., *Nature* **2001,** *412* (6845), 452-455.

73. Hirschberg, J. H. K. K.; Brunsveld, L.; Ramzi, A.; Vekemans, J. A. J. M.; Sijbesma, R. P.; Meijer, E. W., *Nature* **2000,** *407* (6801), 167-170.

74. Barth, J. V.; Weckesser, J.; Trimarchi, G.; Vladimirova, M.; De Vita, A.; Cai, C.; Brune, H.; Gunter, P.; Kern, K., *J. Am. Chem. Soc.* **2002,** *124* (27), 7991-8000.

75. Böhringer, M.; Morgenstern, K.; Schneider, W.-D.; Berndt, R.; Mauri, F.; De Vita, A.; Car, R., *Phys. Rev. Lett.* **1999,** *83* (2), 324.

76. Gong, J.-R.; Wan, L.-J.; Yuan, Q.-H.; Bai, C.-L.; Jude, H.; Stang, P. J., *Proc. Natl. Acad. Sci. U.S.A.* **2005,** *102* (4), 971-974.

77. Yuan, Q.-H.; Wan, L.-J.; Jude, H.; Stang, P. J., *J. Am. Chem. Soc.* **2005,** *127* (46), 16279-16286.

78. Kushvaha, S. S.; Yan, Z.; Xiao, W.; Xu, M.-J.; Xue, Q.-K.; Wang, X.-S., *Nanotechnology* **2007,** *18*, 145501-145511.

79. Safarowsky, C.; Leo Merz, A. R.; Broekmann, P.; Hermann, B. A.; Schalley, C. A., *Angew. Chem., Int. Ed.* **2004,** *43* (10), 1291-1294.

80. Schreiber, F., *J. Phys.: Condens. Matter* **2004,** *16* (28), R881-R900.

81. Thery-Merland, F.; Me'thivier, C.; Pasquinet, E.; Hairault, L.; Pradier, C. M., *Sensors Actuators B* **2006,** *114*, 223-228

82. Whelan, C. M.; Barnes, C. J.; Walker, C. G. H.; Brown, N. M. D., *Surf. Sci.* **1999,** *425* (2-3), 195-211.

83. Vericat, C.; Vela, M. E.; Benitez, G. A.; Gago, J. A. M.; Torrelles, X.; Salvarezza1, R. C., *J. Phys.: Condens. Matter* **2006,** ***18***, R867-R900.

84. Klok, H.-A.; Jolliffe, K. A.; Schauer, C. L.; Prins, L. J.; Spatz, J. P.; Moller, M.; Timmerman, P.; Reinhoudt, D. N., *J. Am. Chem. Soc.* **1999,** *121* (30), 7154-7155.

85. Schonherr, H.; Paraschiv, V.; Zapotoczny, S.; Crego-Calama, M.; Timmerman, P.; Frank, C. W.; Vancso, G. J.; Reinhoudt, D. N., *Proc. Natl. Acad. Sci. U.S.A.* **2002,** *99* (8), 5024-5027.

86. vanManen, H.-J.; Paraschiv, V.; Garcia-Lopez, J. J.; Schonherr, H.; Zapotoczny, S.; Vancso, G. J.; Crego-Calama, M.; Reinhoudt, D. N., *Nano Lett.* **2004,** *4* (3), 441-446.

87. Barth, J. V., *Surf. Sci. Rep.* **2000,** *40* (3-5), 75-149.

88. Schreiber, F., *Prog. Surf. Sci.* **2000,** *65* (5-8), 151-257.

89. Cotton, F. A.; Lin, C.; Murillo, C. A., *Proc. Natl. Acad. Sci. U.S.A.* **2002,** *99* (8), 4810-4813.

90. Eddaoudi, M.; Kim, J.; Vodak, D.; Sudik, A.; Wachter, J.; O'Keeffe, M.; Yaghi, O. M., *Proc. Natl. Acad. Sci. U.S.A.* **2002**, *99* (8), 4900-4904.

91. Holliday, B. J.; Mirkin, C. A., *Angew. Chem., Int. Ed.* **2001,** *40* (1), 2022-2043.

92. Pirondini, L.; Bertolini, F.; Cantadori, B.; Ugozzoli, F.; Massera, C.; Dalcanale, E., *Proc. Natl. Acad. Sci. U.S.A.* **2002,** *99* (8), 4911-4915.

93. Leininger, S.; Olenyuk, B.; Stang, P. J., *Chem. Rev.* **2000,** *100* (3), 853-908.

94. Saalfrank, Rolf W.; Maid, H.; Scheurer, A., *Angew. Chem., Int. Ed.* **2008,** *47* (46), 8794-8824.

95. Perrin, D. D.; Armarego, W. L. F., *Purification of Laboratory Chemicals, 2nd ed.* Pergamon Press: Oxford: 1980.

96. *SMART & SAINT Software Reference Manuals*, 4.0; Siemens Energy & Automation, Inc. Analytical Instrumentation: Madison, Wisconsin, USA, 1996.

97. Sheldrick, G. M. *SADABS: a Software for Empirical Absorption Correction* University of Gottingen, Gottingen, Germany, 1996.

98. *SHELXTL Reference Manual*, 5.03; Siemens Energy & Automation, Inc., Analytical Instrumentation: Madison, Wisconsin, USA, 1996.

99. Connors, K. A., Binding Constants: The Measurement of Molecular Complex Stability. Wiley-Interscience: New York: 1987; pp 24-28.

100. Zhang, K.; Prabhavathy, J.; Yip, J. H. K.; Koh, L. L.; Tan, G. K.; Vittal, J. J., *J. Am. Chem. Soc.* **2003,** *125* (28), 8452-8453.

101. Mukherjee, P. S.; Das, N.; Kryschenko, Y. K.; Arif, A. M.; Stang, P. J., *J. Am. Chem. Soc.* **2004,** *126* (8), 2464-2473.

102. Pan, G.-B.; Liu, J.-M.; Zhang, H.-M.; Wan, L.-J.; Zheng, Q.-Y.; Bai, C.-L., *Angew. Chem., Int. Ed.* **2003,** *42* (24), 2747-2751.

103. Semenov, A.; Spatz, J. P.; Möller, M.; Lehn, J.-M.; Sell, B.; Schubert, D.; Weidl, C. H.; Schubert, U. S., *Angew. Chem., Int. Ed.* **1999,** *38* (17), 2547-2550.

104. Cyr, D. M.; Venkataraman, B.; Flynn, G. W., *Chem. Mater.* **1996,** *8* (8), 1600-1615.

105. Mu, Z.; Shu, L.; Fuchs, H.; Mayor, M.; Chi, L., *J. Am. Chem. Soc.* **2008,** *130* (33), 10840-10841.

106. Carlson, T. A., ***X-ray photoelectron spectroscopy*** Stroudsburg, Pa.: Dowden, Hutchinson & Ross; [New York] : distributed worldwide by Academic Press, 1978.

107. Watts, J. F.; Wolstenholme., J., ***An introduction to surface analysis by XPS and AES*** J. Wiley: New York, NY 2003.

108. Bader, G.; Ashrit, P. V.; Truong, V.-V., *Appl. Opt.* **1998,** *37* (7), 1146-1151.

109. Bader, G.; Ashrit, P. V.; Girouard, F. E.; Trung, V.-V., *Appl. Opt.* **1995,** *34* (10), 1684-1691.

110. Tompkins, H. G.; McGahan., W. A., ***Spectroscopic ellipsometry and reflectometry : a user's guide*** Wiley: New York, 1999.

111. Pekker, D.; Pekker, L., *Thin Solid Films* **2003,** *425* (1-2), 203-209.

112. Baro, A. M.; Miranda, R.; Alaman, J.; Garcia, N.; Binnig, G.; Rohrer, H.; Gerber, C.; Carrascosa, J. L., *Nature* **1985,** *315* (6016), 253-254.

113. Chen., C. J., ***Introduction to scanning tunneling microscopy*** Oxford University Press: New York 1993.

114. Bonnell., D. A., ***Scanning tunneling microscopy and spectroscopy: theory, techniques, and applications*** VCH: New York, 1993.